Universiteit
Leiden
The Netherlands

First light with the 120-lens Dragonfly Spectral Line Mapper

Chen, S.; Lokhorst, D.M.; Pasha, I.; Bowman, W.P.; Janssens, S.R.; Rhea, C.; ... ; Dokkum, P. van

Citation
Chen, S., Lokhorst, D. M., Pasha, I., Bowman, W. P., Janssens, S. R., Rhea, C., … Dokkum, P. van. (2025). First light with the 120-lens Dragonfly Spectral Line Mapper. *Publications Of The Asp*, *137*(8). doi:10.1088/1538-3873/adedb8

Version:	Publisher's Version
License:	Creative Commons CC BY 4.0 license
Downloaded from:	https://hdl.handle.net/1887/4290612

Note: To cite this publication please use the final published version (if applicable).

Publications of the Astronomical Society of the Pacific, 137:084103 (24pp), 2025 August https://doi.org/10.1088/1538-3873/adedb8
© 2025. The Author(s). Published by IOP Publishing Ltd on behalf of the Astronomical Society of the Pacific (ASP).

OPEN ACCESS

First Light with the 120-lens Dragonfly Spectral Line Mapper

Seery Chen[1,2], Deborah M. Lokhorst[3], Imad Pasha[4,5], William P. Bowman[4,5], Steven R. Janssens[4], Carter Rhea[4], Qing Liu[6], Zili Shen[5], Roberto G. Abraham[1,2], and Pieter van Dokkum[5]

[1] David A. Dunlap Department of Astronomy & Astrophysics, University of Toronto, 50 St. George Street, Toronto, ON M5S3H4, Canada
[2] Dunlap Institute, University of Toronto, 50 St. George Street, Toronto, ON M5S3H4, Canada
[3] NRC Herzberg Astronomy & Astrophysics Research Centre, 5071 West Saanich Road, Victoria, BC V9E2E7, Canada
[4] Dragonfly Focused Research Organization, 150 Washington Avenue, Santa Fe, NM 87501, USA
[5] Department of Astronomy, Yale University, 52 Hillhouse Ave., New Haven, CT 06511, USA
[6] Leiden Observatory, Leiden University, Einsteinweg 55, NL-2333 CC, Leiden, The Netherlands
Received 2025 April 17; revised 2025 July 3; accepted 2025 July 8; published 2025 August 7

Abstract

The Dragonfly Spectral Line Mapper (DSLM) is a 120-lens distributed aperture narrowband imaging telescope that is operating as a pathfinder for an upcoming 1140-lens instrument being built to directly image the circumgalactic medium of nearby galaxies. DSLM has been on sky since 2023 October, collecting representative data for individual galaxies in Hα, [O III], and [N II]. In this paper, observations obtained for three targets (NGC 6946, NGC 891, and NGC 7479) are presented. These galaxies span a range of recessional velocities and foreground contamination levels, enabling a comprehensive evaluation of the experimental design. Diffuse Hα structures down to 10^{-19} erg s^{-1} cm^{-2} arcsec^{-2} on 10′ scales are mapped by our data. We report the discovery of new extended structures in diffuse Hα and [N II] emission around NGC 6946 and NGC 891. We also map multiple new structures surrounding NGC 6946; however, due to the low recessional velocity of this object and the significant presence of galactic Hα emission at low galactic latitudes, we cannot confirm whether these gas clouds are associated with NGC 6946 or are of Galactic origin. We present a framework using the "`sbcontrast`" tool which can be broadly applied to evaluate the limiting depth of wide-field narrowband imaging observations. The surface brightness limits obtained with DSLM are consistent with our theoretical predictions and, in fields with low foreground contamination, the imaging depth is not limited by instrument systematics. Future dedicated surveys on galaxies selected by recessional velocity to avoid sky emission lines are projected to reach surface brightness limits of 10^{-20} erg s^{-1} cm^{-2} arcsec^{-2} on scales of a few arcmin, placing the circumgalactic medium of nearby galaxies within reach.

Unified Astronomy Thesaurus concepts: Optical telescopes (1174); Circumgalactic medium (1879)

1. Introduction

The Dragonfly Spectral Line Mapper (DSLM) is a novel narrowband imaging telescope array designed to map line emission at surface brightness levels an order of magnitude deeper than conventional wide-field narrowband imaging telescopes. The instrument consists of an array of 120 commercial Canon telephoto lenses operating together as a distributed aperture refractor telescope. The entrance pupil of each element of the array contains a full-aperture ultra narrow bandpass (0.8 nm) interference filter. The filters are tilt-tunable, allowing the DSLM to adapt to the differing recessional velocities of its targets, so it can operate as a narrow-bandpass integral field spectrometer with a resolving power of $R \sim 800$. DSLM therefore combines the groundbreaking low surface brightness imaging ability of the Dragonfly Telephoto array (Abraham & van Dokkum 2014) with a narrow bandpass imaging spectroscopic capability. The instrument concept was proven with a 3-lens pathfinder, which discovered a giant shell of ionized gas in the outskirts of M82 (Lokhorst et al. 2022). With its current filter set, the array probes diffuse gas out to a recessional velocity of 3800 km s^{-1}. In the 120-lens CCD-based configuration described here, DSLM is equivalent to a 1.6 m aperture $f/0.26$ telescope, with a $2.^{\circ}4 \times 1.^{\circ}9$ field of view (FOV; Chen et al. 2024).

The key to DSLM's design is the Dragonfly "Filter-Tilter," which holds the filter in front of each lens and tilts the filter to change the central wavelength, using the property of interference filters wherein central wavelength is a function of incidence angle (Lokhorst et al. 2020).[7] DSLM is equipped with "science" and "offband" filters. The science filters have a

Original content from this work may be used under the terms of the Creative Commons Attribution 4.0 licence. Any further distribution of this work must maintain attribution to the author(s) and the title of the work, journal citation and DOI.

[7] Placing the filter at the front of all the optics is crucial when combining a very narrow filter bandpass with a fast optical design, because interference filter performance degrades sharply in a converging beam. With filters ahead of the lens optics, the beam entering the filters is perfectly collimated with a focal ratio of infinity, so the filter retains its narrow bandpass and high transmission.

0.8 nm bandpass targeting the Hα λ6563, [N II] λ6583 and [O III] λ5007 lines (hereafter refered to as Hα, [N II], and [O III] unless otherwised specified). By tilting the filters between 0° and 20°, the effective central bandpass is shifted to match the wavelength of emission lines at the recessional velocity of the target of interest. This enables the same Hα filter to image both the H$\alpha\lambda$6563 and [N II] λ6583 lines individually. The offband filters are used for continuum subtraction. These have a bandpass of 30 nm with central wavelengths to the "left" and "right" of the science filters in wavelength space. We refer the interested reader to Chen et al. (2022) for more details on the filter design.

DSLM is capable of observing nearby galaxies within the local volume out to distances of 50 Mpc; the filters can be tilt-tuned to observe Hα emission from objects at recessional velocities between $-700 < v < 3800\,\mathrm{km\,s^{-1}}$. However, the array's design is optimal for observing galaxies in the velocity range $1200 < v < 2800\,\mathrm{km\,s^{-1}}$ for the following reasons: (1) There are significant empty windows in the distribution of airglow sky lines in this range and exploiting these gaps provides optimal imaging depth, (2) the expected angular sizes of the virial radii of nearby galaxies decreases with distance and is best matched to the DSLM FOV within this range (e.g., for a Milky Way mass halo, the virial radius is $11\overset{\circ}{.}5$ at $D = 1$ Mpc and $0\overset{\circ}{.}5$ at $D = 20$ Mpc), (3) [N II] imaging (undertaken with the same filter as Hα imaging) is only possible up to a recessional velocity of $2800\,\mathrm{km\,s^{-1}}$, and (4) the "spectral acceptance FOV" (SAF) of the instrument (i.e., the FOV where the line of interest falls within the bandpass of the filter) increases with distance; at $v \approx 1200\,\mathrm{km\,s^{-1}}$ the SAF is ≈73% of the total FOV, which increases to 100% by $v \approx 2600\,\mathrm{km\,s^{-1}}$. The last of these effects is described in further detail in Appendix A.

In this paper we present the first three DSLM commissioning targets: NGC 6946, NGC 891, and NGC 7479. These three targets cover a broad range of environments and observing conditions. While NGC 6946 and NGC 891 are outside of the "optimal" recessional velocity window for DSLM, these are still velocities which DSLM can observe at, and these targets were chosen for two reasons. First to test how DSLM and the preliminary data reduction pipeline performs targeting lower recessional velocities, and second, because these are well studied galaxies with a plethora of H II features to compare surface surface brightness depths with. We give brief summaries of the targets selected below.

1. NGC 6946 (the "Fireworks Galaxy") is a nearly face-on (30° inclination) spiral galaxy, with a recessional velocity of $40\,\mathrm{km\,s^{-1}}$ (Bekiaris et al. 2016). Lying approximately $11\overset{\circ}{.}7$ off of the galactic plane, NGC 6946 is in an area of the sky that is rich in foreground cirrus and local galactic Hα emission. This galaxy is well studied across the electromagnetic spectrum, with observations in radio (Boomsma et al. 2008), infrared (Bigiel et al. 2020), Hα (Cedres et al. 2012), ultraviolet (Yadav et al. 2021), and X-ray (Holt et al. 2003) wavelengths, to list only a few of the myriad of investigations of this well-known object. NGC 6946 is not an optimal target for DSLM when searching for circumgalactic gas around galaxies, as it has a very low recessional velocity and bright foreground structures covering much of its field that make it difficult to distinguish between Milky Way foreground line emission and emission originating at the target. The high filter tilt required for lower velocity targets (see Appendix A for more information) also introduces a large variation in the bandpass across the FOV.
2. NGC 891 is an edge-on spiral galaxy with a recessional velocity of $528\,\mathrm{km\,s^{-1}}$ (Falco et al. 1999). It lies $17\overset{\circ}{.}4$ below the galactic plane and is also in an area with significant galactic foreground. NGC 891 is also a very well studied galaxy with numerous detections in H I (Sancisi & Allen 1979; Oosterloo et al. 2007), in Hα (Dettmar 1990; Rand 1997), and in X-ray (Strickland et al. 2004), to list a few. Some more notable studies include Fraternali & Binney (2008) using the neutral gas dynamics of NGC 891 to infer the need for accretion onto the galaxy, and S. Das et al. (2024) potentially detecting diffuse H I emission in the CGM around NGC 891. As with NGC 6946, the recessional velocity is low enough that the bandpass varies significantly across the FOV, but emission from the Milky Way and NGC 891 can be better distinguished because of the galaxy's larger recessional velocity.
3. NGC 7479 is a barred spiral galaxy with a recessional velocity of $2376\,\mathrm{km\,s^{-1}}$ (Huchra et al. 1999). The galactic foreground is not empty in this field, but it is straightforward to separate Milky Way Hα emission from that related to NGC 7479 due to the large recessional velocity of NGC 7479. The wavelength of Hα emission at the recessional velocity of NGC 7479 is not coincident with any prominent sky lines, which yields a lower sky background. This object is an example of a target with recessional velocity and galactic latitude that is well-suited for observations with DSLM.

The outline for this paper is as follows. In Section 2, we describe the DLSM observations yielding the data presented in this paper. The specialized data reduction procedure used to process these data is described in Section 3. In Section 4, we present our results: Hα maps for the three aforementioned galaxies, the surface brightness limits reached in these maps, as well as [N II]/Hα and [O III]/Hα line ratio maps. In Section 5, we discuss new structures discovered, reflect on instrument performance, and discuss how the data collected by

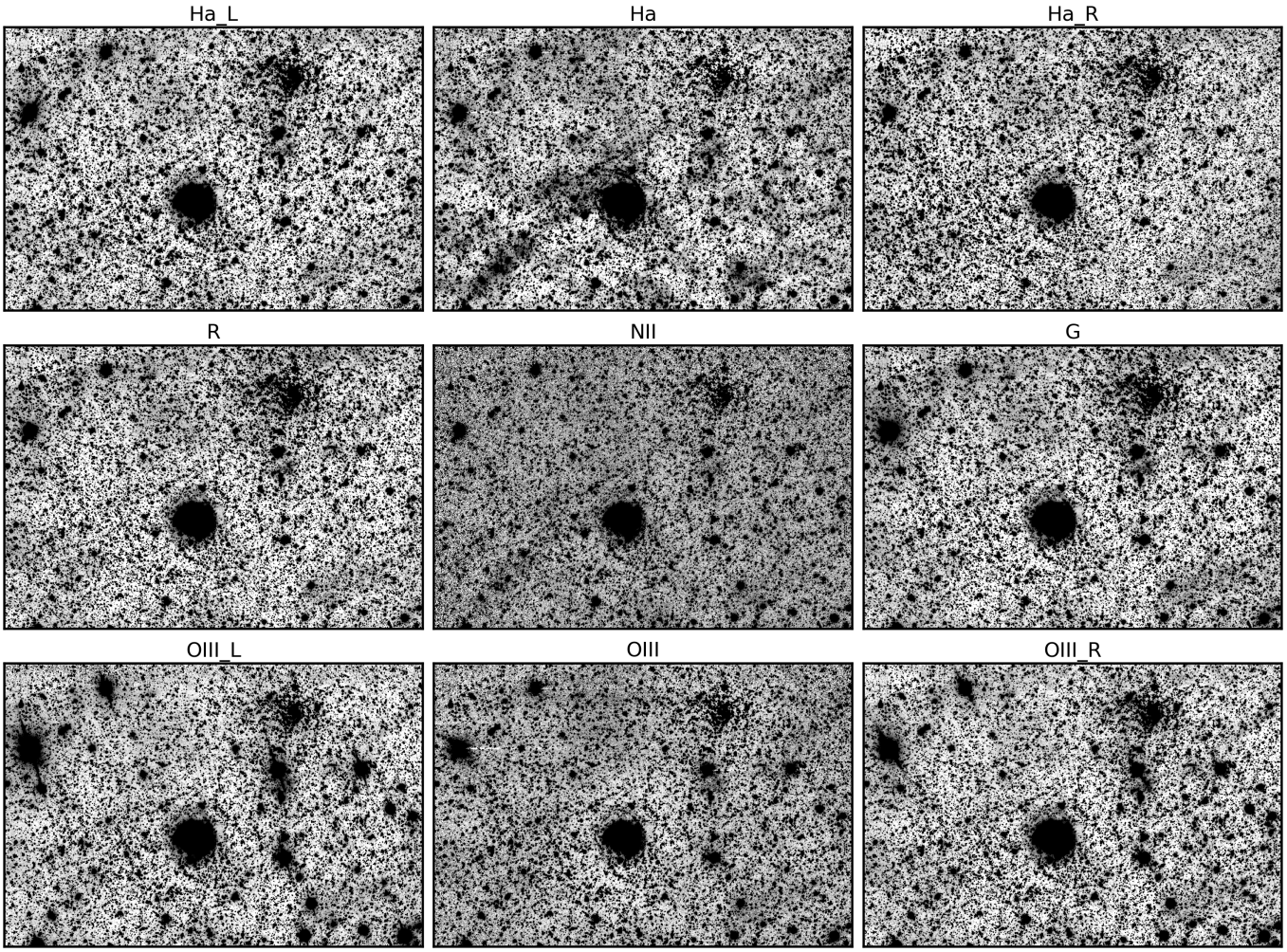

Figure 1. Observations of NGC 6946 ($v = 40$ km s^{-1}) collected through all filters on DSLM, together with r and g stacks from the broadband Dragonfly-48 array, are displayed. The field of view shown in each panel is approximately $1.^{\circ}5 \times 1^{\circ}$, with right ascension running horizontally. The second column shows the deep narrowband data obtained by DSLM targeting Hα, [N II] and [O III] emission, respectively. The first and third columns show the data sets used to remove the continuum from the narrowband observations. Note that the Hα left and Hα right continuum filters are used to remove the background from both the Hα and [N II] data (the Hα and [N II] data are collected by the same filter at different tilts, i.e., both the Hα and [N II] lines are between the Hα left and Hα right continuum filters).

the 120-lens DSLM informs the construction of the 1140-lens array.

2. Observations

DSLM is located in Mayhill, New Mexico, at New Mexico Skies Observatories. The reader is referred to Chen et al. (2024) for a detailed description of DSLM beyond the summary given here. Narrowband imaging targeting Hα, [N II], and [O III] emission line wavelengths together with medium bandpass continuum imaging of NGC 6946, NGC 891, and NGC 7479 were collected from 2024 March to 2024 October. During this seven-month period, commissioning data gathered on several targets were collected on 114 nights while the array was being assembled. We used 900 s exposure times for narrowband observations, and 400 s exposure times for medium bandpass observations (for continuum subtraction), with 2×2 on-chip binning for both cases. Due to the narrowness of the filter bandpass, narrowband observations were barely sky-noise limited (sky noise ~ 5 e$^-$, read noise ~ 4.5 e$^-$) in 900 s, and longer integration times would have resulted in a higher signal-to-noise stack. However, our planned active flexure compensation system has not yet been implemented, so exposure times were limited to 900 s to avoid losing frames due to internal flexure in the array.[8] The background is also elevated by around 50%

[8] The upcoming 1140-lens array will use low read noise CMOS sensors. As a result, images will be fully sky-noise limited in 600 s even though the effective pixel size will be 2.5× smaller than the $4.''74$ pixels (when binned 2×2) of the setup described here.

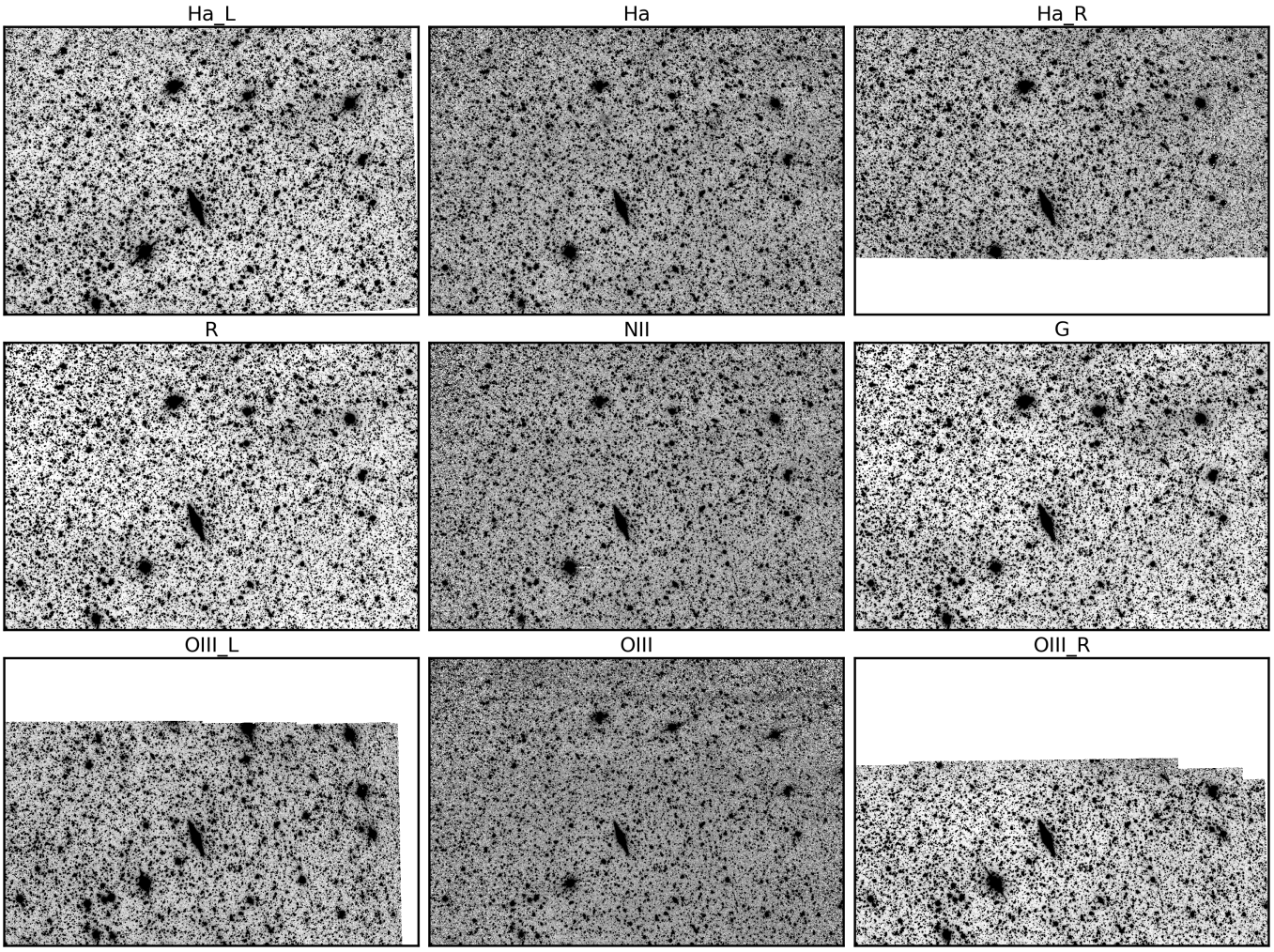

Figure 2. As for Figure 1, except for NGC 891 ($v = 528$ km s^{-1}).

in these data due to a thermal leak; see Appendix B for further details. For NGC 6946 and NGC 891, we also obtained broadband images in SDSS *g*-band and *r*-band filters using the 48-lens broadband Dragonfly Telephoto Array.

Each night, four dark frames were taken for each lens unit, with exposure times matching those of the science frames. These are used to create a nightly master dark frame for each unit. If no master dark for a given unit on a given night was made due to image quality issues, interruptions in observing, or any other reason, the master dark of the closest date was used. Master flat-field images were created for each lens unit by tilt-tuning to wavelengths that are in between sky lines. This avoids introducing large background variation in the field due to the sky lines falling within the filter bandpass. We use master sky flats from data collected in 2024 October for the reduction of the science data for the three targets. For each target, we select the set of master flats with the filter tilt angle closest to the target tilt angle to minimize the impact of flat field variations introduced by a dependence on tilt angle (Lokhorst et al. 2022).

3. Data Reduction

The data reduction procedure largely follows that used to reduce data from the three-lens DSLM pathfinder (Lokhorst et al. 2022), which itself is based on the pipeline used for the reduction of Dragonfly broadband data (Danieli et al. 2020). Individual frames were dark subtracted, flat fielded, assessed for image quality, sky subtracted, checked for the zeropoint and tilt, then resampled. The sky subtraction technique differs from that used in the DSLM pathfinder data reduction pipeline, and is described in Appendix B. Image quality checks were implemented throughout, and a median stack was assembled from frames that passed all data quality checks. Referencing this median stack, masks of bad pixels were made for each frame that passed all data quality checks. Then these masked

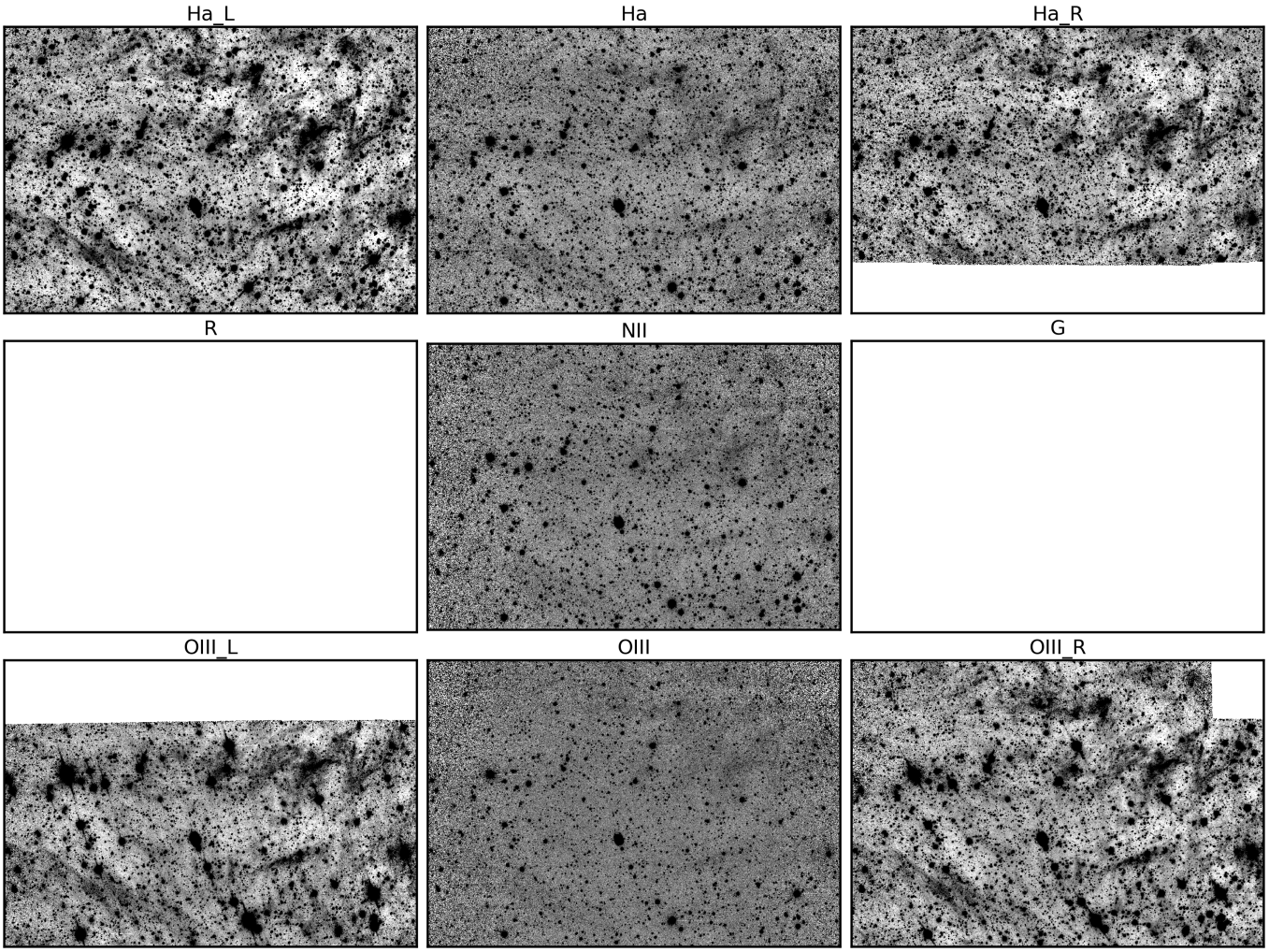

Figure 3. As for Figures 1 and 2, except for NGC 7479 ($v = 2376$ km s^{-1}). Note that g and r-band images are unavailable in this field. Prominent "stripes" of galactic cirrus are seen in the medium band images, which correspond to faint structures seen in the narrowband data. As described in the text, the imprint of these structures is successfully removed by our continuum subtraction procedure.

frames were used to construct the final stack using a weighted average. Figures 1, 2, and 3 show the final coadded stacks for each target in all available filters.

3.1. Continuum Subtraction

Data collected with Hα left and right medium-band filters were obtained simultaneously with the Hα and [N II] narrowband observations, and were used to continuum subtract the Hα and [N II] data with the following procedure. First, the medium band data were normalized using an interactive procedure to determine a normalization factor that best subtracts non-saturated stars from the Hα frames. Normalizations for the left and right filters were obtained independently. Next, these normalized frames were averaged to obtain the final normalized continuum frame. Finally, this normalized continuum was subtracted from the Ha narrowband image. This procedure was also used to continuum subtract the [O III] data with the corresponding [O III] left and right medium-band images.

Due to the random dither in the lens pointing locations, the medium-band data occasionally did not fully overlap the narrowband imaging footprint. When insufficient coverage was present in either the left or right medium-band filter data sets, data from a single filter with sufficient coverage was used. These cases are shown in Figures 2 and 3. This had little impact on the interpretation of our observations, since all calibrations frames had significant overlap with the targets of interest.

3.2. Flux Calibration

To flux calibrate the final stacked images, stars were matched to their counterparts in the APASS catalog (Henden

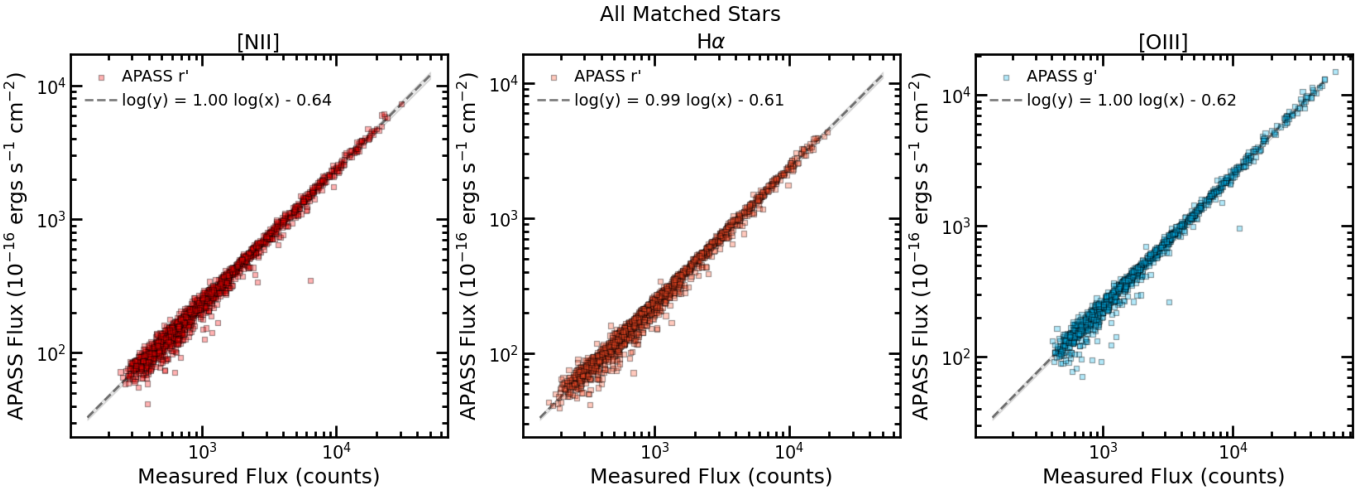

Figure 4. Flux calibration of the NGC 7479 field for our [N II], Hα, and [O III] stacks, using the stellar fluxes in Sloan r or g band from the APASS catalog. Each square point represents a star detected in the final stack, where the measured flux is the stellar flux in counts we derive from aperture photometry of our data, and the APASS flux is r (or g) band flux of the star in the APASS catalog scaled to the width of our filters, 0.8 nm. A linear fit in log-log space is shown by the dashed line. See text for details.

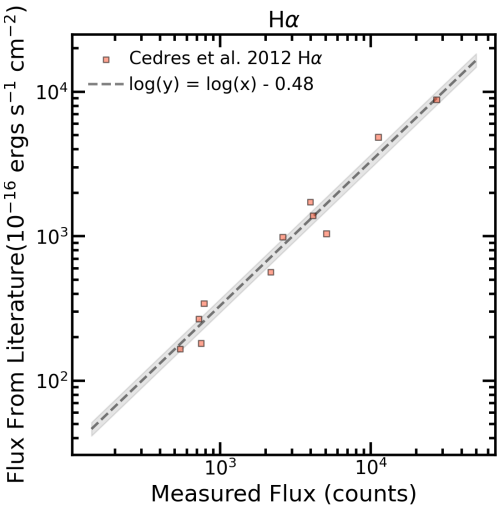

Figure 5. Cross check of flux calibration with H II regions in the NGC 6946 field for our Hα data stack, using Hα flux from Cedres et al. (2012). Each square point represents a H II region identified in the continuum subtracted data stack, where the measured flux is the sum of counts in the H II region and the literature flux is the sum of all Hα sources from Cedres et al. (2012) within the area covered by the DSLM H II region. The linear fit while constraining the slope to unity is show by the dashed line, with the 90 percent confidence in fit shown by the gray region.

et al. 2016). For the Hα and [N II] images, the r-band stellar fluxes from the APASS catalog were scaled by the width of the filters to obtain the expected summed flux within the filter bandpass. This calculation was made under the assumption that the SDSS r-band filter used for the APASS r-band catalog is a top-hat function and that the stars have a flat continuum across the r-band filter bandpass. A stellar catalog was then created by running Source Extractor (Bertin & Arnouts 1996) on the image, and a comparison was performed. For [O III], the fluxes were matched to APASS g-band data. A linear fit was then performed for flux in units of 10^{-16} erg s^{-1} cm^{-2} versus counts, with results shown in Figure 4. This procedure yields the following flux calibration:

$$\log_{10}(F\ [10^{-16}\mathrm{erg\,s^{-1}cm^{-2}}]) = a\ \log_{10}(F\ [\mathrm{counts}]) + b \quad (1)$$

where $a = 1.00 \pm 0.01$ and $b = -0.61 \pm 0.03$ for the Hα, [N II], and [O III] images. The same flux calibration was obtained for all targets.

A verification of the flux calibration was performed using an alternative technique that compares the fluxes of H II regions in NGC 6946 to published measurements in the literature. The DSLM data resolution is lower than that of the data used to create published H II region catalogs, so the calibration obtained in this way is best viewed as a sanity check on the procedure described in the previous section. The comparison was performed by summing the flux of adjacent H II regions measured by Cedres et al. (2012) to effectively "bin" to match the scale of the H II regions in the DSLM data. The fluxes of eleven H II regions in the Hα continuum-subtracted NGC 6946 image were compared to the literature via this method and, following Equation (1), values of $a = 1.00 \pm 0.1$ and $b = -0.53 \pm 0.3$ were found when the slope was allowed to vary. When the slope was fixed at $a = 1$, the y-intercept was found to be $b = -0.48 \pm 0.05$. These results are shown in Figure 5. The difference between the flux calibration using stars and H II regions was approximately 20%, which is conservatively adopted as the uncertainty in following absolute flux measurements.

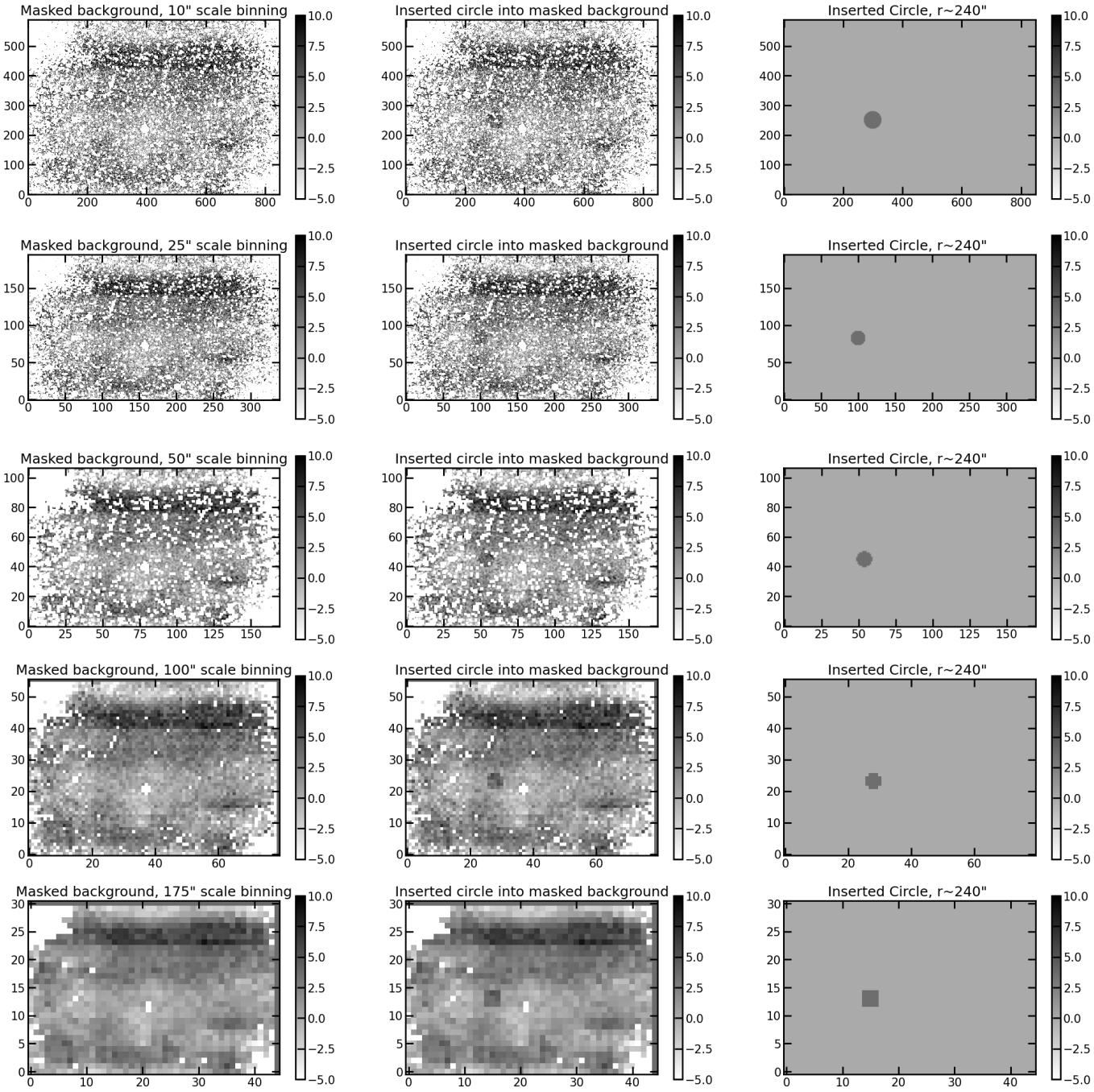

Figure 6. Left column: the masked and binned background of the NGC 7479 continuum subtracted data stack used by `sbcontrast` to calculate the surface brightness limit at a given scale. Middle column: the respective masked background image with a circle at 3σ surface brightness at $240''$ inserted in the image. Right column: the inserted 3σ circle. The colorbar is in units of 10^{-18} erg s^{-1} cm^{-2} arcsec^{-2}. The dark strip across the top is due to sky subtraction residuals.

4. Results

4.1. Surface Brightness Limits

The observations reported here were obtained to test the effectiveness of the instrument concept and a key objective of this paper is to present the limiting surface brightness achievable by DSLM. We adopt the `sbcontrast` method to calculate the surface brightness limit (Keim et al. 2022).

The `sbcontrast` method defines the surface brightness limit as the contrast between a region of a specified spatial

Table 1
Summary of Surface Brightness Limits for the Continuum Subtracted Hα Coadds

Target	Number of Hα Frames in Stack	Hα 3σ sbcontrast Limit (per pixel −4.″74) (erg s^{-1} cm^{-2} arcsec^{-2})	Hα3σ sbcontrast limit (100″) (erg s^{-1} cm^{-2} arcsec^{-2})
NGC 6946	2585	4.4×10^{-18}	9.3×10^{-19}
NGC 891	733	8.1×10^{-18}	7.7×10^{-19}
NGC 7479	1112	5.6×10^{-18}	3.8×10^{-19}

Note. Individual Hα narrowband frames have a 900 s exposure time, and offbands frames are 400 s. The surface brightness limit calculated with sbcontrast is given in erg s^{-1} cm^{-2} arcsec^{-2} at individual pixel (4.″74) and 100″ scale features.

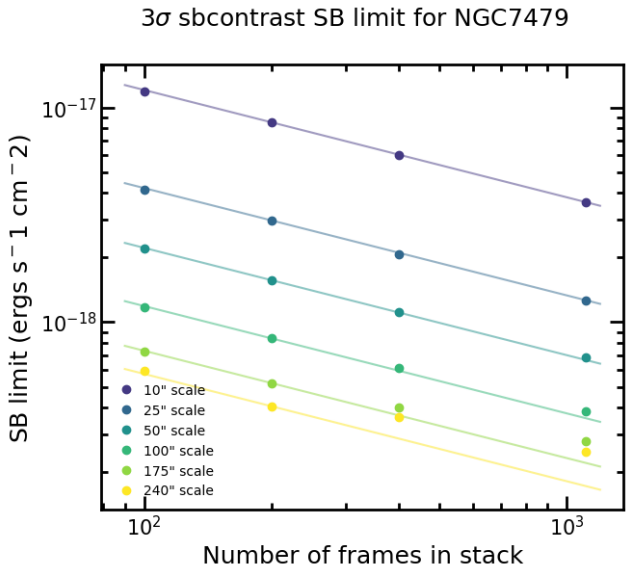

Figure 7. 3σ Hα surface brightness limit calculated with sbcontrast for coadded stacks of 100, 200, 400, and 1112 frames of the NGC 7479 field, at varying scales sizes. Lines showing the expected Poisson noise behavior of decreasing as $\sqrt{N}$, where N is the number of frames, matched to the surface brightness limit at 200 frames, are shown to guide the eye.

scale and its immediate surroundings. This approach is well-suited for detecting low-surface brightness objects of a given size against a locally smooth background that may exhibit variations on much larger scales. By using this definition, two common challenges in surface brightness limit estimation are avoided: first, it eliminates the need to extrapolate from smaller scales to the scale of interest; and second, it ensures that the measurement remains unaffected by large-scale gradients in the image. A visual example of the intermediate step of sbcontrast binning on varing scales, and what a 3σ surface brightness limit feature looks like inserted into the image, is shown in Figure 6.

We ran the sbcontrast code on our final continuum subtracted image stacks and the results are presented in Table 1. The meaning of the limits presented in this table are best understood from Figure 7, which shows the surface brightness limit in the NGC 7479 field (the galaxy with highest recessional velocity, hence least contaminated by Galactic foregrounds) as a function of the number of frames in a stack, with different colored lines corresponding to different scales used to calculate the surface brightness limit. This figure is edifying because the Poissonian assumption of noise reducing as the square root of the exposure time corresponds to a straight line in the right hand panel of this figure. In this particular field, the Poissonian assumption holds until the we reach the largest scales (4′). For NGC 6946 and NGC 891, the Poissonian assumption breaks at smaller scales due to these fields being more crowded with low surface brightness Hα emission. This is shown in Figure 8, where the NGC 6946 field, which is very rich in low surface brightness Hα, breaks from the Poisson assumption at smaller scales than NGC 891. There is real low surface brightness emission on these scales, but our reduction code is not currently designed to recover it, and sbcontrast confirms that we cannot distinguish real structures on these scales from foreground systematics, or from artifacts from our data reduction process. This is why the 3σ Hα surface brightness limits on 100″ scales given in Table 1 for NGC 891 and NGC 6946 are much higher than one would expect compared to NGC 7479 given the number of frames in the image stack. However, the main message is that at smaller scales ($\lesssim$2′), our depth is not limited by any systematics.

4.2. New Structures Seen in the Hα Maps of NGC 6946, NGC 891, and NGC 7479

The continuum subtracted Hα image of NGC 6946, NGC 891, and NGC 7479 are shown in Figures 9, 10, and 11 respectively. These images are masked to remove residuals from bright sources (excluding known galaxies) in the field, with the masked regions replaced by the local sky background value.

For NGC 6946, previously imaged Hα emission around the galaxy appears clearly in the image. We see the extended upper double arm of the galaxy imaged by Ferguson et al. (1998) in Hα, and find the upper arm to extend further than previously detected. In particular, we detect an extended Hα

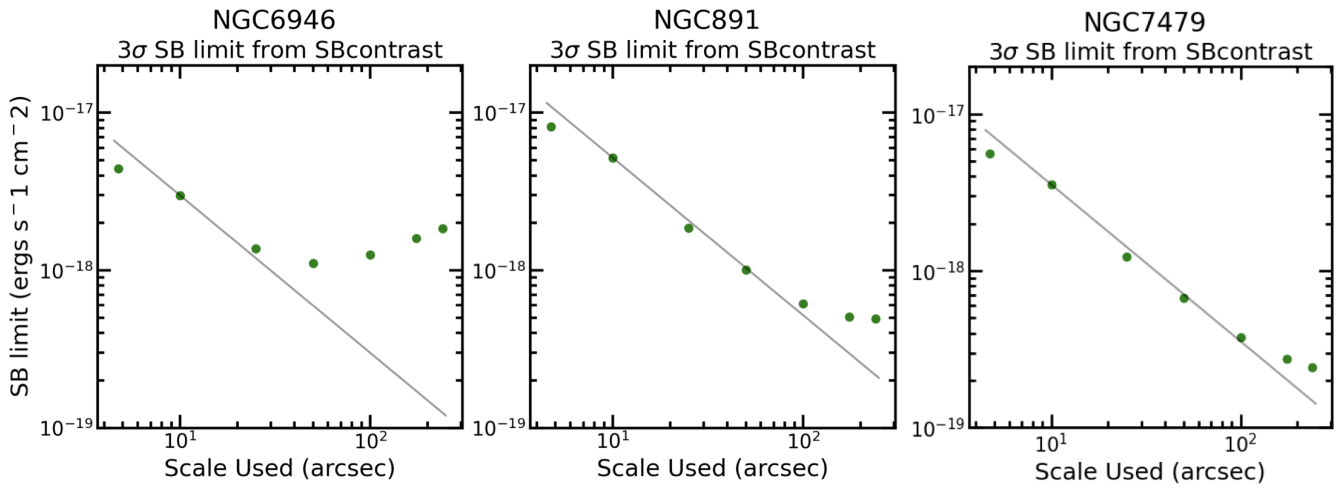

Figure 8. 3σ Hα surface brightness limits calculated with `sbcontrast` for the coadded stacks of the NGC 6946, NGC 891, and NGC 7479 field, at varying scales sizes. Note, this differs from Figure 7 which plots the surface brightness limit against number of frames in a coadded stack. The number of frames in the coadded stack used to derive these surface brightness limits are given in Table 1. Lines showing Poissonian noise behavior of decreasing as $\sqrt{N}$ are shown to guide the eye, where N is area of a feature at a given scale (or $\sqrt{N}$ is the scale length), matched to the surface brightness limit at 10″ scale. NGC 7479 best follows Poissonian noise behavior, with slight deviation beyond 100″. See text for details of why NGC 6946 and NGC 891 do not follow Poissonian noise behavior.

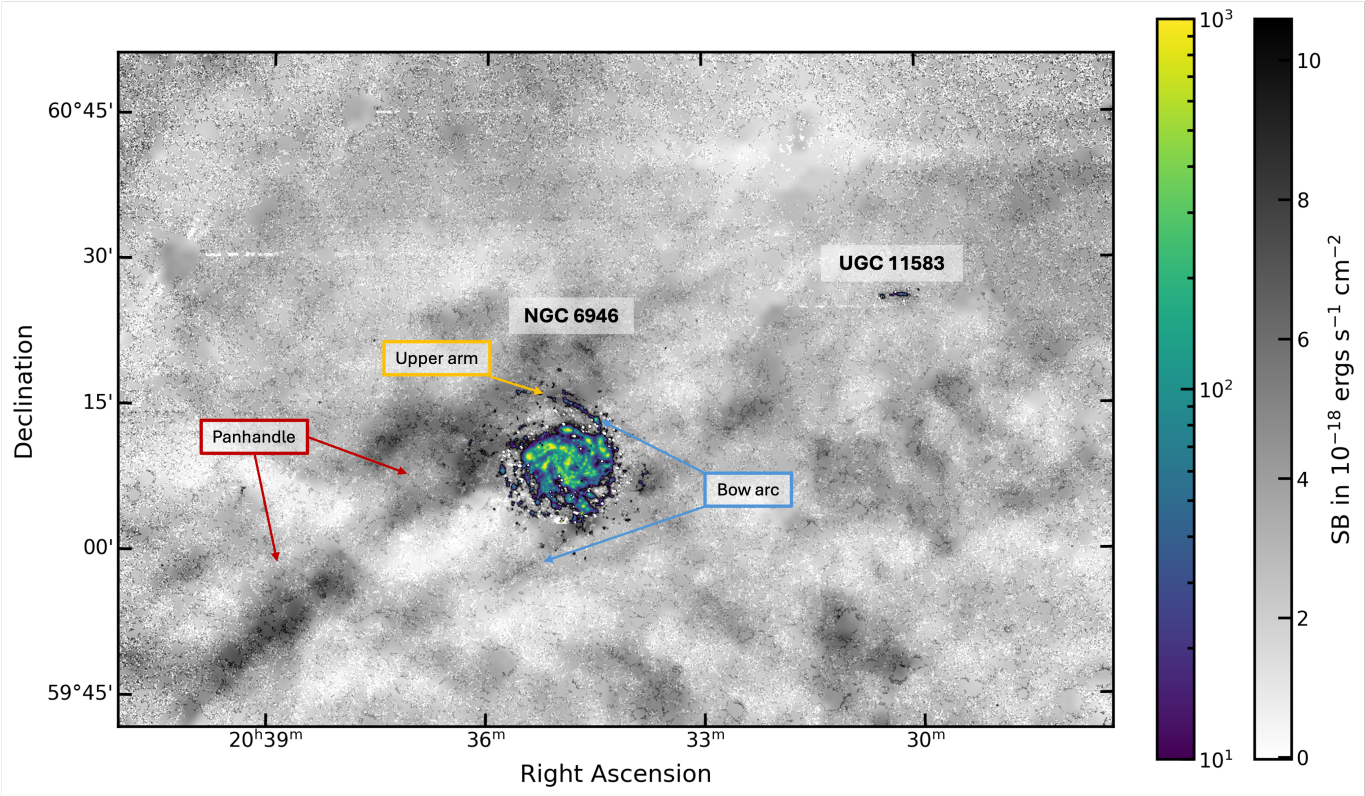

Figure 9. DSLM Hα map of NGC 6946 and UGC 11583, continuum-subtracted and masked. Masked regions are replaced with the local median of unmasked background pixels. Colorbars show the scaling of the Hα surface brightness in units of 10^{-18} erg s^{-1} cm^{-2} arcsec^{-2}, the grayscale is in a liner scale to show the low surface brightness features, the viridis overploted is in log scale to show the brighter compact features. Colored annotations label the various features in the image. The "panhandle" labeled in red curves off the top of the galaxy. The upper arm labeled in yellow is comprised of compact Hα regions extending beyond the galaxy's disk. The diffuse Hα feature extending from the right side of the galaxy to the lower left appears to form a bow shock shaped arc when connected to the upper arm, this is labeled in blue as the "Bow arc."

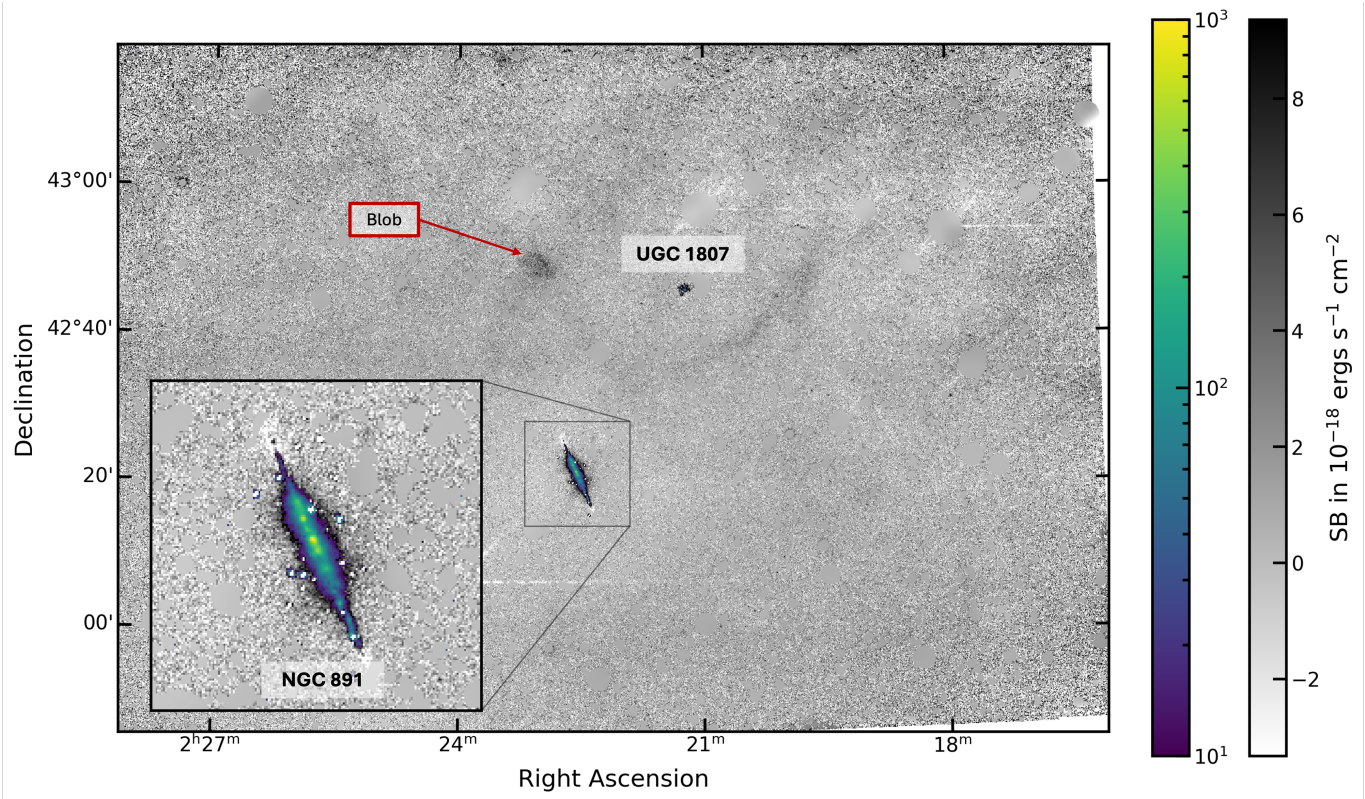

Figure 10. DSLM Hα map of NGC 891, continuum-subtracted and masked. Masked regions are replaced with the median of unmasked background pixels. An inset in the bottom left corner shows a zoom in on the galaxy to better show the H II regions inside the galaxy, with the same scaling as the outer plot. The colorbar shows the surface brightness flux in units of 10^{-18} erg s^{-1} cm^{-2} arcsec^{-2}. The new feature discovered in this field that we call the "blob" is labeled in red.

feature extending from the right side of the galaxy to the lower left that appears to connect to the arm identified by Ferguson et al. (1998), which now appears to form an arc (resembling a bow wave) when connected to the upper arm. This feature is labeled in blue as the "Bow arc" in Figure 9. Furthermore, we detect previously unknown diffuse Hα structures covering this entire field, with the most notable being a structure (the "panhandle") that appears to connect to the north east of the galaxy, following the outer upper double arms down to the south east. However, given the low recessional velocity of the galaxy, we cannot exclude the possibility that this structure is a chance projection of structures in the foreground. Given the relatively high surface brightness of this feature (see below) we think the foreground interpretation more likely than that it is a bright component of the circumgalactic medium. We discuss this in further detail in Section 5.2.

The panhandle has an average surface brightness of approximately 5.4 $\times$ 10^{-18} erg s^{-1} cm^{-2} arcsec^{-2} with the brightest sections at approximately 8.3 $\times$ 10^{-18} erg s^{-1} cm^{-2} arcsec^{-2}. It is about $0\overset{\circ}{.}8$ in length and $0\overset{\circ}{.}07$–$0\overset{\circ}{.}2$ in width, subtending an area of approximately 250 arcmin^2. Line ratio maps of those feature will be presented in the next section.

For NGC 891 with its dwarf companion UGC 1807, we find two notable Hα emission features: the "blob" above NGC 891 and the "swoop" which appears to connect to the "blob" forming an arc below UGC 1807. We find diffuse extraplanar Hα emission off of the NGC 891 disk, and find this emission to appear slightly clumpy rather than smooth. Due to the changing bandpass across the FOV effect at higher tilts, with NGC 891 at a recessional velocity of 528 km s^{-1}, the blob is in a location of the frame where the bandpass includes that of zero recessional velocity.

For NGC 7479, we see many previously detected compact H II regions within the galaxy, but no extended diffuse emission in this field. The abundant diffuse galactic foreground continuum emission subtracts away very cleanly (see Figure 3 for a comparison). Although this field lacks diffuse emission of interest, the flat background makes it a ideal field to calculate surface brightness limiting depths.

4.3. Line Ratio Maps with [N II] and [O III]

The continuum subtracted [N II] and [O III] images of NGC 6946 are shown in Figure 12. Bright sources excluding known galaxies are masked and replaced with the local sky

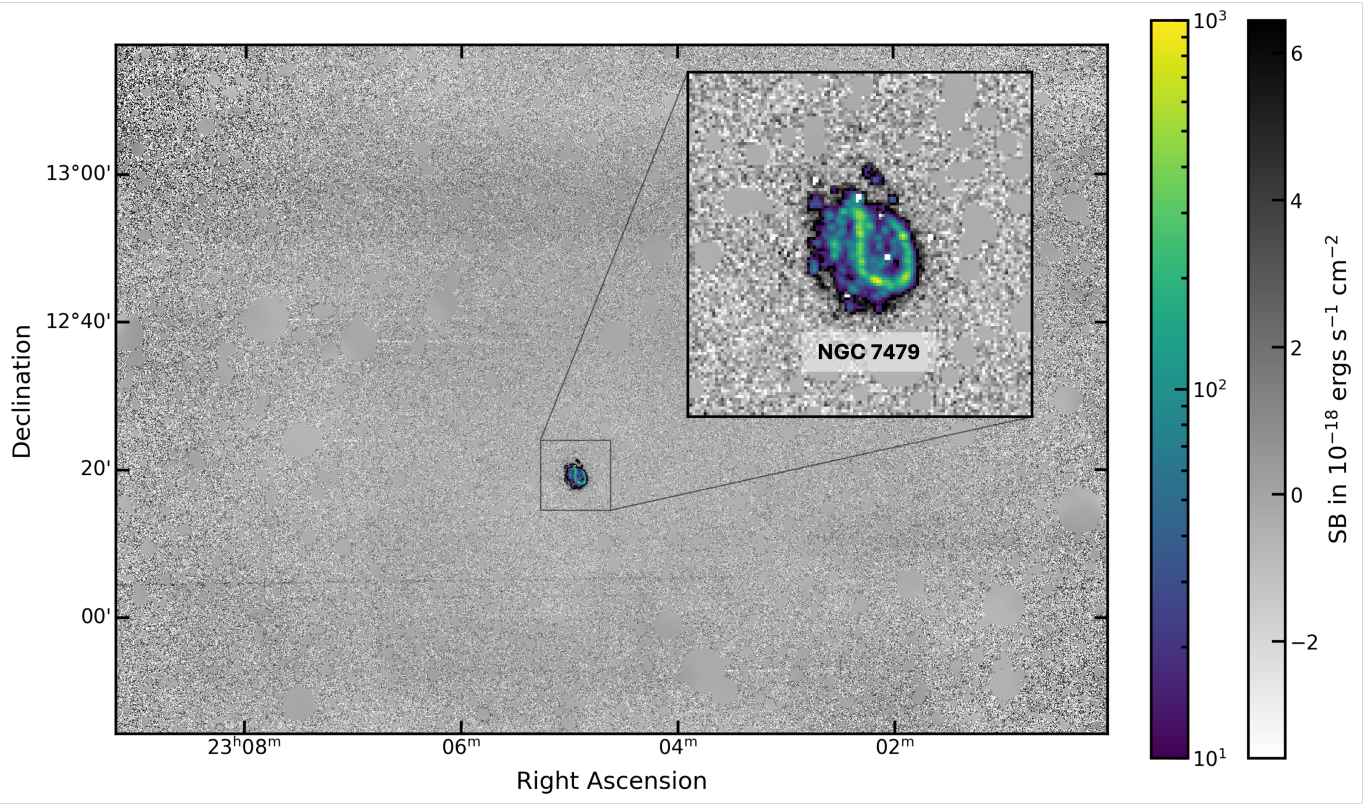

Figure 11. DSLM Hα map of NGC 7479, continuum-subtracted and masked, with the outskirts scaled to optimally show background structure in grayscale, and the center of the galaxy in log scale to show compact structure in color. Masked regions are replaced with the local median of unmasked background pixels. An inset in the upper right corner shows a zoom in on the galaxy, with the same scaling as the outer plot. Color bars show the surface brightness flux in scaling in units of 10^{-18} erg s^{-1} cm^{-2} arcsec^{-2}.

background value, then the images were binned 4×4. Various diffuse structures are seen in [N II] such as the panhandle, with [N II]/H$\alpha \approx 0.5$ on average. However these diffuse structures are not detected in [O III]. Zooming into the galaxy, the line ratio maps in Figure 13 show the upper arm is barely detected in [N II], but moderately in [O III], indicative of lower metallicity gas in star-forming H II regions. Interpretation of these line ratio maps is further elaborated on in Section 5.1. The line ratio zoom-in maps for NGC 891 and NGC 7479 are included in Figures 14 and 15 respectively for completeness, but the full FOV versions of these maps are not presented as the lack of features detected in [N II] and [O III] at large radii result in uninformative maps.

5. Discussion

The observations presented here were designed to characterize the performance of DSLM by exploring objects at a range of recessional velocities and foreground contamination levels. Even though these observations are relatively "shallow" by the standards of the upcoming 1140 lens Dragonfly array, corresponding to approximately 10 minutes integrations with that instrument, they are deeper than any wide-field narrowband imaging undertaken in these fields previously. We compare DSLM imaging depth between targets as well as with other Hα observations in the literature in this section. Additionally, the DSLM data have revealed some interesting features that are worth understanding in greater detail. We will focus on two of these here, namely the "panhandle" in the target field of NGC 6946 and the "blob" seen in the observations of NGC 891.

5.1. Imaging Depth Comparisons

In the NGC 6946 field, the deepest comparable Hα imaging in the literature is from Ferguson et al. (1998), which reach a surface brightness limit below 3×10^{-17} erg s^{-1} cm^{-2} arcsec^{-2}.[9] The resolution of this data set at $0\farcs69$ pixels, with approximately $1\farcs2$ seeing at KPNO, is higher than DSLM which has $4\farcs74$ pixels in the configuration used in this paper (not seeing limited). The FOV of in Ferguson et al. (1998) is smaller at $21' \times 21'$, compared to the $2\fdg4 \times 1\fdg9$ FOV of DSLM. Amateur astrophotography with long integration times on small telescopes have

[9] The exact surface brightness limit is not specified, but this is the typical threshold they quote for detecting H II regions in their data.

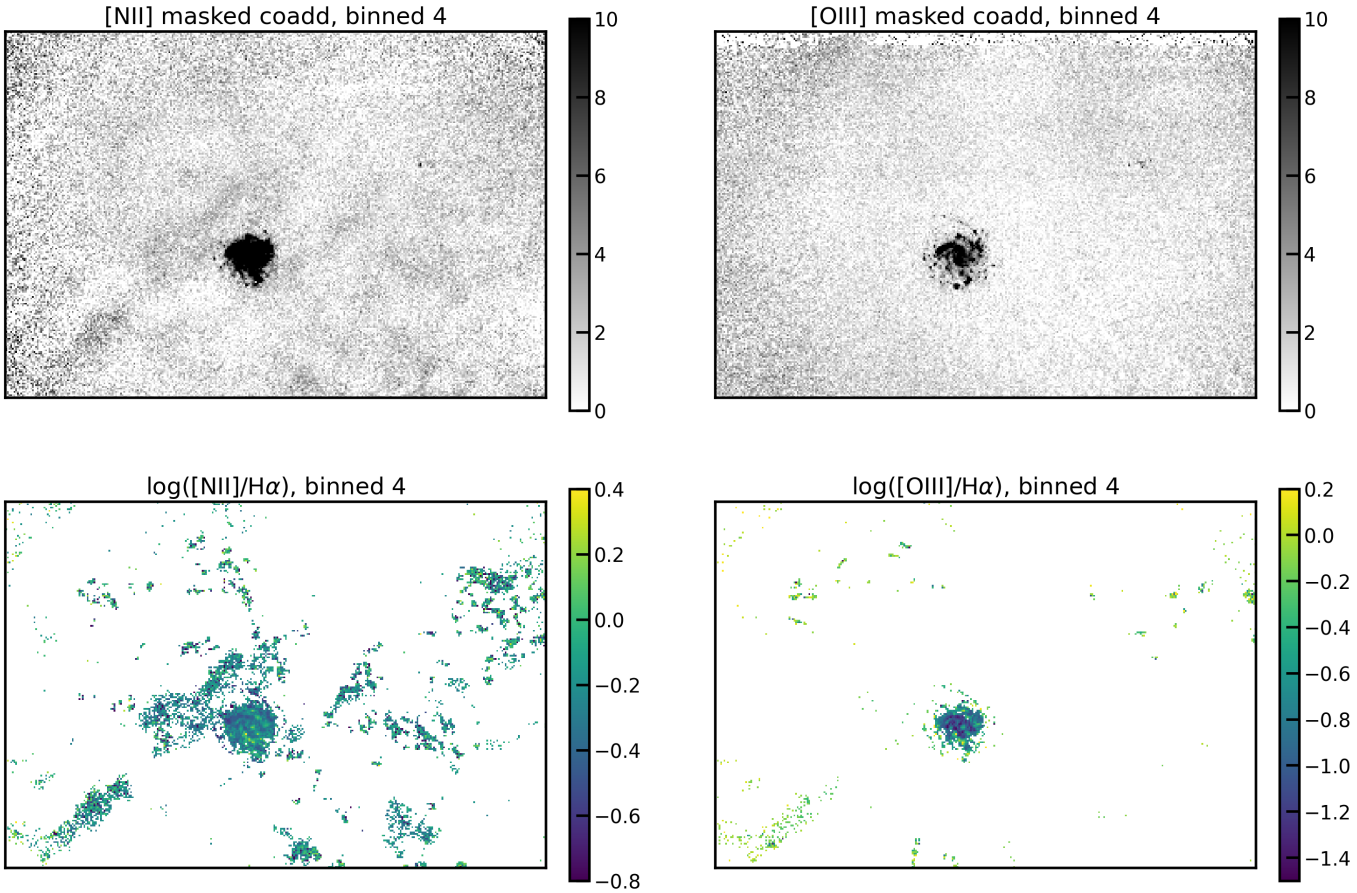

Figure 12. Upper left: DSLM [N II] λ6583 map of NGC 6946 and UGC 11583, continuum subtracted, masked, and binned 4 × 4 where the value of each binned pixel is from the median of the pixels that are combined to make each binned pixel. The masked regions are replaced with the local median of unmasked background pixels. Lower Left: flux ratio map of the [N II] λ6583 emission line flux to the Hα λ6563 emission line flux in the NGC 6946 field. The map is log-scaled. Regions of low signal-to-noise in Hα and [N II] (or Hα and[O III] for the image in the lower right) Upper and Lower Right: same as their respective images on the left but for the [O III] λ5007 line.

reached similar or deeper depths as Ferguson et al. (1998), albeit at lower resolution, with multi degree squared FOVs, making for a more similar comparison to DSLM data. However, the lack of transparency in data reduction methods make it difficult to quantitatively determine surface brightness limits.

Similarly with NGC 891, the deepest Hα imaging in the literature has higher resolution and a much smaller FOV. For NGC 891, Rand et al. (1990) reach a per pixel 1σ sensitivity of EM = 6.5 pc cm^{-6} (assuming $T = 10^4$), equivalent to a surface brightness of 1.3 × 10^{-17} erg s^{-1} cm^{-2} arcsec^{-2}. With a pixel size of 1.″2, assuming Poisson noise, this corresponds to a 3σ sensitivity of 9.9 × 10^{-18} erg s^{-1} cm^{-2} arcsec^{-2} at 4.″74 scales to match the pixel scale of DSLM. Comparatively, DSLM reaches a 3σ sensitivity of 8.1 × 10^{-18} erg s^{-1} cm^{-2} arcsec^{-2} on 4.″74 scales as previously given by Table 1. While not a one-to-one comparison between the two sensitivity limits as the methods for calculating them differ, it is clear both through this, and visually in Figure 10, that the surface brightness depths are comparable.

5.2. *Origin of the Panhandle near NGC 6946*

At first glance, the morphology of the panhandle suggests that the feature is associated with NGC 6946. The diffuse emission appears to extend off of the upper arm of H II regions. However, due to the low recessional velocity, it is difficult to distinguish if the Hα features we see are physically around NGC 6946 or foreground Galactic contamination seen in projection. No Galactic high velocity gas is seen in H I near NGC 6946 by Westmeier (2018) closer than approximately 2°, apart from one cloud that is exactly centered on the galaxy, see Figure 16. The gas that is within a few degrees of NGC 6946 does not appear to have any correlation with the structure of diffuse Hα seen in our Hα map. This does not rule out the panhandle as an High Velocity Cloud (HVC) like object, as the HVC map from

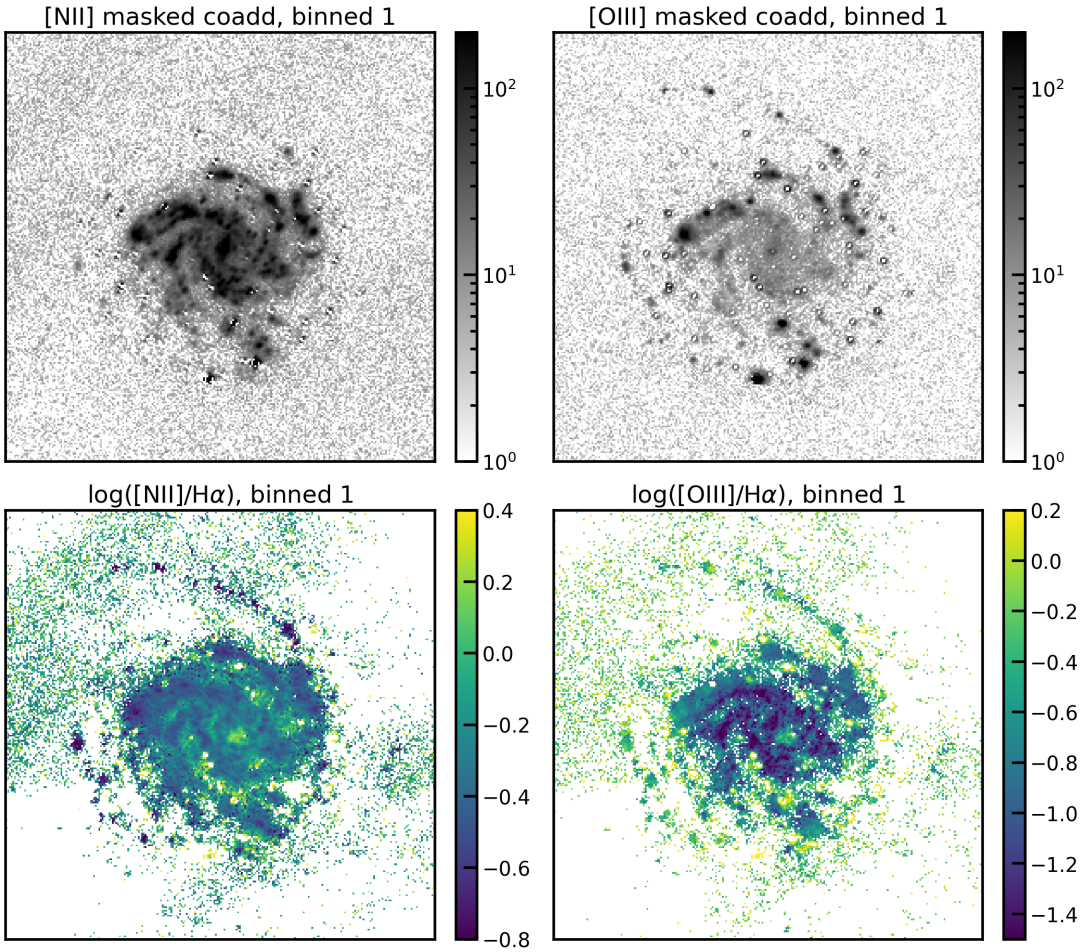

Figure 13. Same as Figure 12 but cropped to better show NGC 6946 and not binned. Note that stars near the center of the galaxy are not masked, and the imperfect continuum subtraction leads to donut shaped residuals present in the image.

Westmeier (2018) lacks the resolution to detect this structure, and it is also possible that the gas has a high ionization fraction and is below the detectable limit in H I. If the panhandle is physically located within our galaxy, then total luminosity varies largely with the distance, from 0.1 to 10 kpc, this corresponds to approximately 10^{31} to $\times 10^{35}$ erg s^{-1}.

NGC 6946 is close enough to the galactic plane that there is significant Hα emission observed in the field by lower resolution galactic Hα surveys such as Wisconsin Hα Mapper (WHAM; Haffner et al. 2003). Figure 17 shows the integrated WHAM Hα data with a rectangle indicating the DSLM footprint. Large scale filamentary structures exist around this field, so it is quite possible that the panhandle is simply a smaller scale filamentary structure below the resolution/detection limit of WHAM.

While the less likely explanation, we explore the implications of the panhandle discovery if it is indeed a structure physically around NGC 6946. The panhandle with a Hα flux of 5.4×10^{-18} erg s^{-1} cm^{-2} arcsec^{-2}, corresponds to a photoionization rate of $\Gamma = 5.9 \times 10^{-12}$ s^{-1} assuming spherical geometry, see detailed calculations in Appendix C. This is around two orders of magnitude higher than what is predicted for the UVB by simulations (Faucher-Giguère et al. 2009; Haardt & Madau 2012; Khaire & Srianand 2019; Faucher-Giguère 2020) with $\Gamma = 2$–5×10^{-14} s^{-1}, and the lower limit from observation (Fumagalli et al. 2017), so another source of ionization is required. The brightness of the panhandle alone can not be used to rule out an association with NGC 6946, as other ionization mechanisms can operate on large scales, like shocks. However, the lack of [O III] detection along with the moderate detection in [N II] makes it unlikely to be shock ionized. 1D theoretical shock models (Morisset et al. 2015) predict it is possible at high shock velocities (>600 km s^{-1}) and weak magnetic fields (<0.01 μG) to have elevated [N II] and low [O III] below the detection limit of our data. While the the magnetic field strength of the circumgalactic medium is not tightly constrained, observations estimate it to be of the order 0.1–1 μG (Lan & Prochaska 2020;

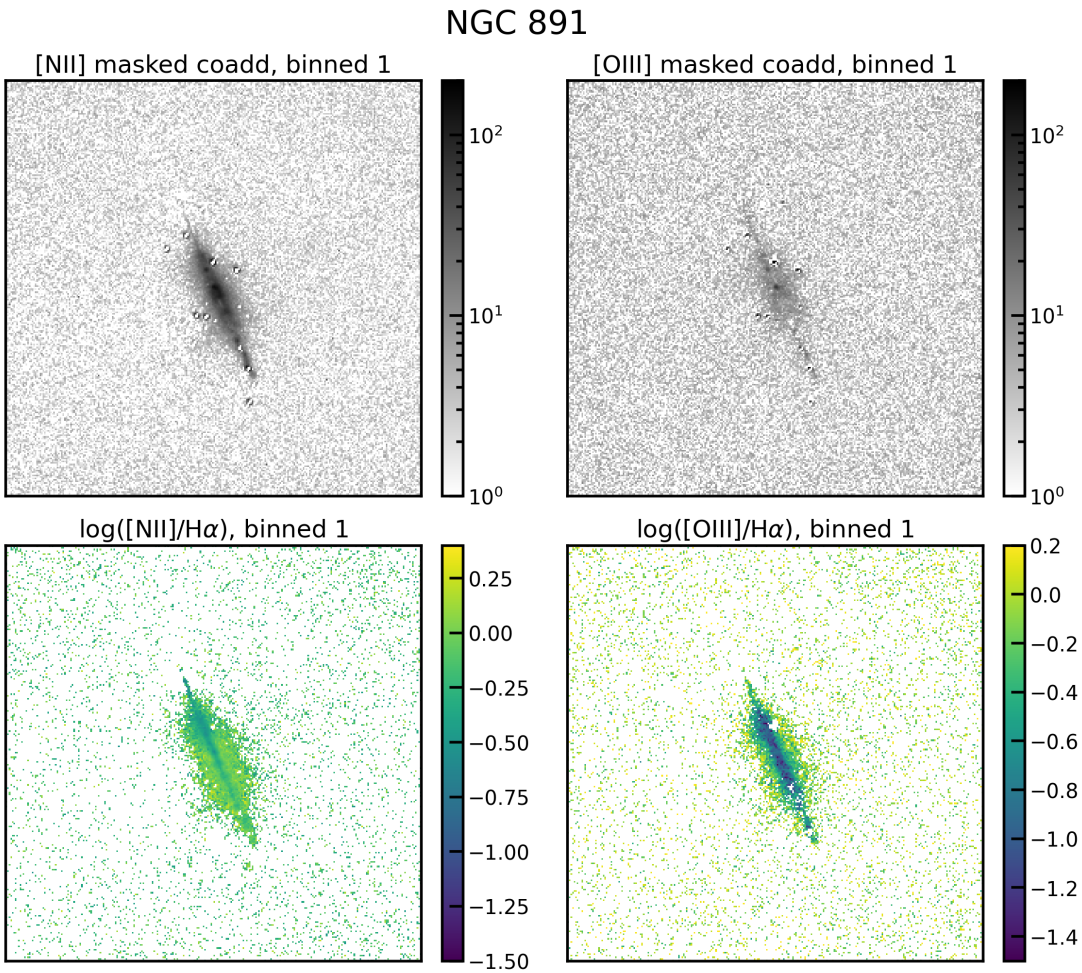

Figure 14. Same as Figure 13 but for NGC 891.

Pakmor et al. 2020; Heesen et al. 2023), and at these magnetic field strengths theoretical shock models predict detectable [O III] from the panhandle in our data. Thus, in this case, the preponderance of evidence strongly indicates that the feature is Galactic.

The uncertainties in the line ratios are large at low surface brightnesses in the narrowband imaging. Wide slit or IFU spectroscopic data is highly complementary to the DSLM data as it allows for better calibration of the relative flux in the DSLM data between Hα, [N II], and [O III] at low surface brightness by extrapolating from line ratios in the spectra, as well as include other optical emission and absorption line diagnostics for features of interest.

5.3. Origin of the Blob near NGC 891

We observed the "blob" in the NGC 891 field with the Low Resolution Imager and Spectrometer (LRIS; Oke et al. 1995) on the Keck I telescope, to determine whether it is associated with NGC 891 or ionized gas in the Milky Way. Two 900 s on-target exposures were obtained on 2024 November 28, in good conditions. Additionally, three blank sky exposures were taken, bracketing the two science exposures. The 831 lines mm^{-1} grating, blazed at 8200 Å, was used in combination with the 1.″0 longslit. The data were reduced using standard techniques. A sky frame was created from the three blank field exposures and subtracted from the science exposures. Cosmic rays were identified by comparing the pixel fluxes in the two science frames. Wavelength calibration was performed using a sky emission line spectrum, obtained from ESO's `skycalc` tool.[10]

The spectrum in the region around Hα is shown in Figure 18. Two sky line residuals are marked. The Hα λ6563, [N II] λ6583, and [S II] $\lambda\lambda$6716, 6731 lines are clearly detected. The radial velocity is 58 $\pm$ 20 km s^{-1}. As shown in the Appendix (Figure 19), this velocity is within the

[10] https://www.eso.org/observing/etc/skycalc/

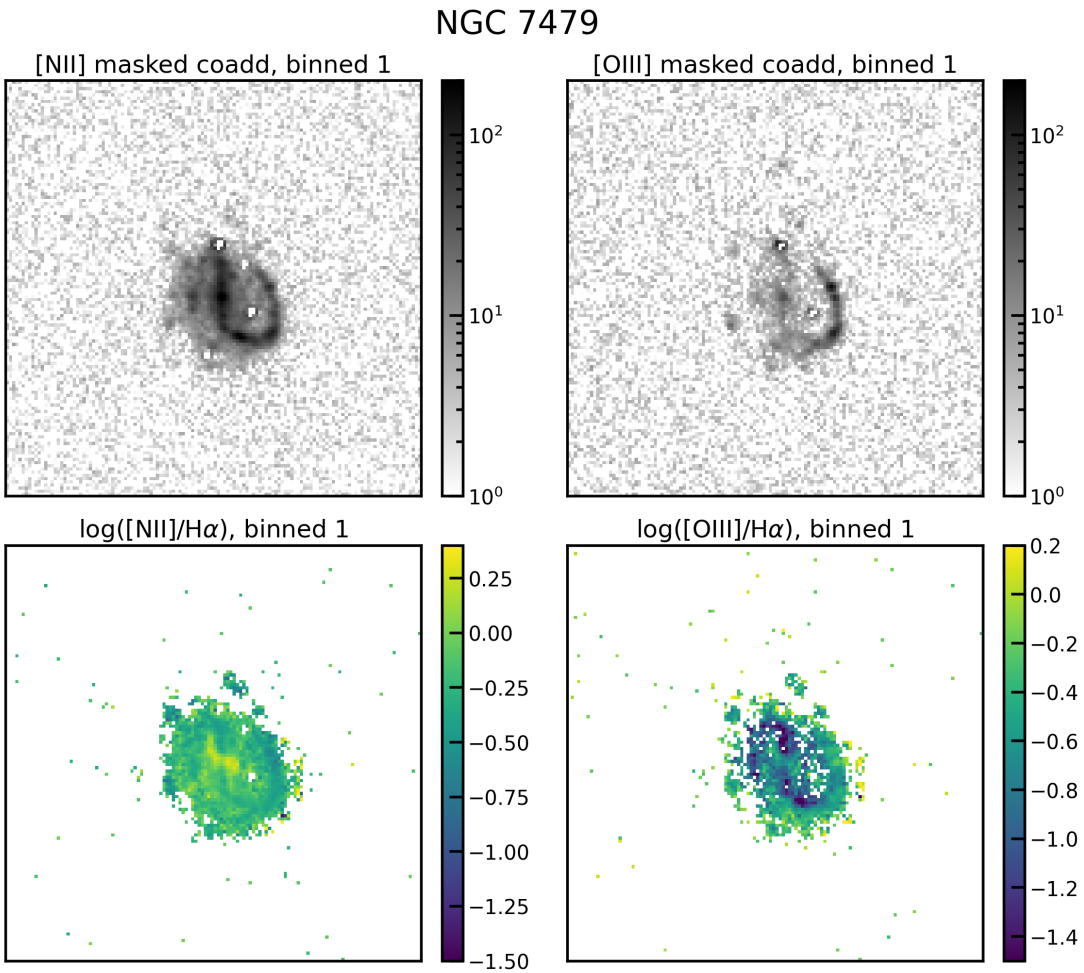

Figure 15. Same as Figure 13 but for NGC 7479.

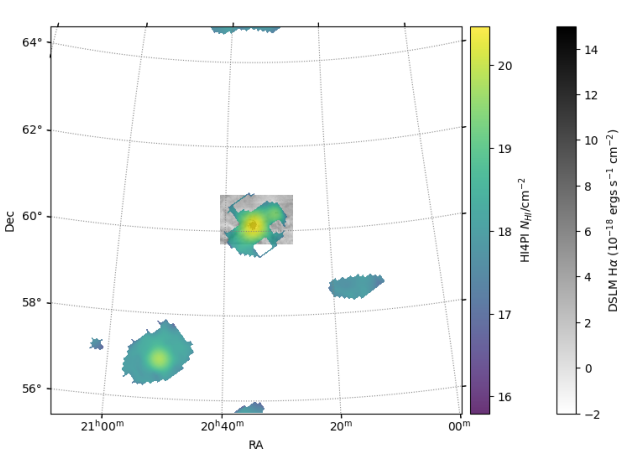

Figure 16. H I column density map of high velocity gas from Westmeier (2018), zoomed into the region around NGC 6946, over plotting the DSLM Hα map.

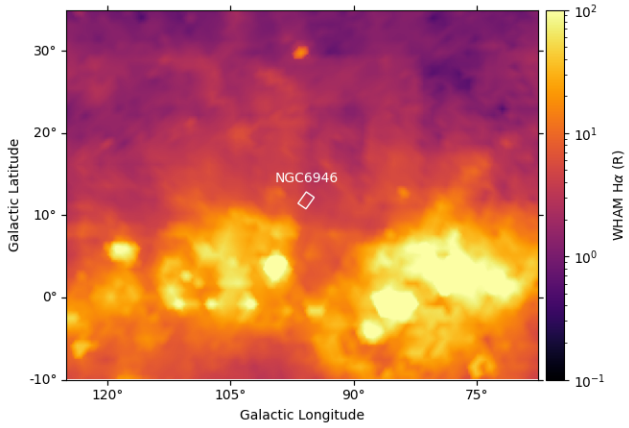

Figure 17. Integrated galactic Hα emission map from WHAM (Haffner et al. 2003), with surface brightness units in Rayleighs, cropped to the area surrounding NGC 6946. The footprint of the DSLM map of NGC 6946 is shown by the white box.

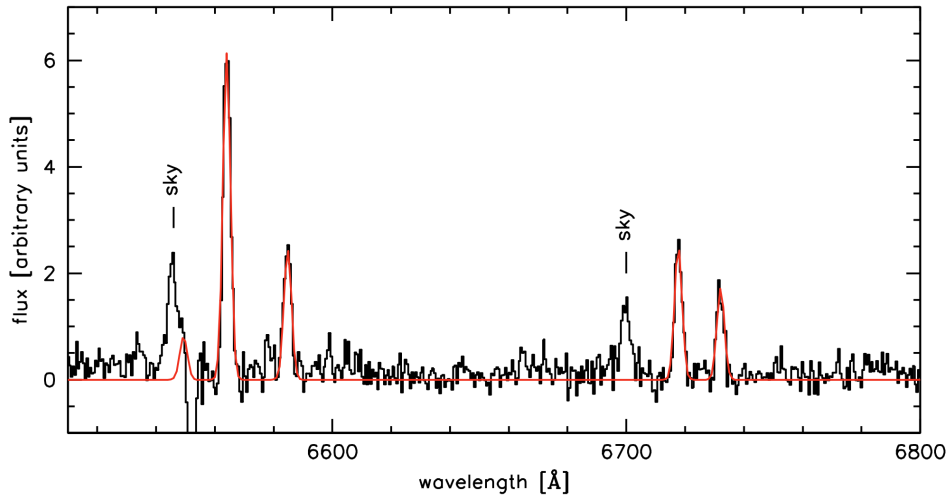

Figure 18. 1D Keck LRIS spectra of the NGC 891 Hα blob, obtained to confirm the existence of the blob and provide basic parameters including recessional velocity and relative [N II], [S II], and Hα line fluxes. The black line shows the resulting spectra after sky subtraction, with sky line residuals labeled as "sky." The best fit model shown in red corresponds to a recessional velocity of $58 \pm 20\,\mathrm{km\,s^{-1}}$.

filter bandpass for the position of the object in the field. NGC 891's radial velocity is $528\,\mathrm{km\,s^{-1}}$, and we conclude that the "blob" is Galactic, and not associated with NGC 891.

While a galactic "blob" is less exciting (in the context of CGM science) than one physically around NGC 891, this discovery points to the importance of considering the non monochromatic FOV when working with DSLM data, especially at lower recessional velocities (higher tilts). The blob is around 30′ north of NGC 891, and this offset corresponds to the bandpass shifting by $-200\,\mathrm{km\,s^{-1}}$ from the target location. With a 0.8 nm filter bandpass corresponding to approximately $400\,\mathrm{km\,s^{-1}}$, the galactic Hα shifts into the edge of bandpass here. This effect can also be seen in the increase of faint background structures north of the galaxy, and a lack of such structures south of the galaxy. The NGC 891 field, like the NGC 6946 field, is also close to the galactic plane and in an area with significant Hα emission. This effect can also be seen in the NGC 6946 Hα map in Figure 9, where toward the top of the field, the diffuse Hα in the field becomes fainter north of the target as the bandpass is shifted blue-wards of the $\sim 0\,\mathrm{km\,s^{-1}}$ gas.

DSLM equipped with Hα filters with a central wavelength closer to the rest frame Hα wavelength would be an excellent instrument to detect galactic Hα features $\sim 5''$ to 10s of arcmin in scale. While DSLM is capable of zero recessional velocity observations (as shown by the NGC 6946 field), the current filter set is not optimized for it.

5.4. Comparing DSLM and DSLM-pathfinder Imaging Depths

Extrapolating from the surface brightness limited reached with the pathfinder and 3 nm filters in Lokhorst et al. (2022), the surface brightness limits presented in Table 1 are consistent with expectations given the number of frames in the data stack. Making the simple assumption that the sky is 3.75 times brighter in the 3 nm pathfinder filter than our current 0.8 nm filter (based on the UVES sky spectrum, from Hanuschik 2003) and assuming we are sky noise limited, we would expect to reach $5.1 \times 10^{-19}\,\mathrm{erg\,s^{-1}\,cm^{-2}\,arcsec^{-2}}$ with 1112 frames. We actually reach $3.8 \times 10^{-19}\,\mathrm{erg\,s^{-1}\,cm^{-2}\,arcsec^{-2}}$ in our 1112 frame Hα stack. The discrepancy can be explained by the fact that the sky background is not flat in wavelength space, and Hα at the recessional velocity of NGC 7479 is not near a sky line. With a filter width of 0.8 nm, the average sky background in a field varies by over 50% as the central wavelength varies between 664.7 and 655.8 nm tilting from 0° to 20° (see Appendix B for more information). Comparing the sky background with a 3 nm filter centered on 657.62 (for imaging M82 in Hα), and the sky background with a 0.8 nm filter centered on 661.85 (for imaging NGC 7479 in Hα), the sky would be 7.6 times brighter in the 3 nm filter imaging M82 than the 0.8 nm filter imaging NGC 7479. Taking this into account, the expected surface brightness limit extrapolating from M82 pathfinder data would then be $3.6 \times 10^{-19}\,\mathrm{erg\,s^{-1}\,cm^{-2}\,arcsec^{-2}}$ which is much closer to the $3.8 \times 10^{-19}\,\mathrm{erg\,s^{-1}\,cm^{-2}\,arcsec^{-2}}$ surface brightness limit we estimate from our data of NGC 7479. The small discrepancy can easily be attributed to uncertainty in flux calibration, or the fact that the 1800 s exposures with the 3 nm filter were sky limited and the 900 s exposures with the 0.8 nm filter were barely sky limited. Additionally, the thermal leak present in the 0.8 nm bandpass filter data contributed about 50% of the sky background. By implementing the known solution to the thermal leak (a UVIR filter in the back of the lens), future data will have significantly less background. With the current CCD cameras, this would mean we are no longer Poisson noise limited. The

CMOS cameras have superior noise characteristics and as such the upgraded DSLM will be sky noise limited.

5.5. Setting the Stage for an 1140-lens DSLM

The data obtained on NGC 7479 reaches the surface brightness limit expected from the number of frames taken, but we do not see extended diffuse emission around this object. This is not surprising, as the depth obtained does not reach the $\approx 10^{-20}$ erg s^{-1} cm^{-2} arcsec^{-2} threshold that Lokhorst et al. (2019) estimate is needed to directly image the circumgalactic medium of Milky Way-mass galaxies. Our imaging was not limited by any systematics on this target, achieving surface brightness depths limited only by the integration time we were able to devote to the observations. We did not go deeper simply because we were limited by the amount of usable data collected while commissioning the instrument, whose purpose was to test concepts for an even larger instrument. S. Chen et. al (2025, in preparation) will describe the lessons learned from the first year of operation of the 120-lens array, and describe how our solutions to these issues resulted in improvements[11] that informed the design of the upcoming 1140-lens Dragonfly Telephoto Array now under construction in Chile.

6. Conclusion

We present observations of three galaxies (NGC 6946, NGC 891, and NGC 7479) used to commission the 120 lens version of the DSLM. These data are the deepest wide-field narrowband observations ever obtained on these targets, and reveal a number of new diffuse Hα emission structures, reaching down to surface brightness sensitivities around 10^{-19} erg s^{-1} cm^{-2} arcsec^{-2} on 100″ scales. Using the `sbcontrast` method, we show that these limits correspond to the surface brightness sensitivity limits expected from the instrument's experimental design. In between sky lines, where DSLM is not limited by any sources of systematic error, the surface brightness limit increases with integration time and has not reached a noise floor. The next stage in the evolution of the DSLM is growing the instrument from a 120-lens array to a 1140-lens array with improved sensors, to enable imaging at surface brightness levels below 10^{-20} erg s^{-1} cm^{-2} arcsec^{-2} over large areas of the sky. Construction of this upgraded array has already begun. The upgraded array will be the equivalent of a 4.7 m aperture $f/0.09$ refractor. With this upgraded array, the data from all three targets presented in this paper would be reproducible in only 30 minutes of observing time. In the same way that lessons learned from the 3-lens DSLM-pathfinder allowed the 120-lens DSLM described here to be successfully built, the lessons learned from the 120-lens DSLM inform the construction and operation of the 1140-lens version array. The ultimate scaling limits of mosaic telescope arrays are not known, and until they are reached, the array may continue to grow in size.

[11] For example, a large number of frames were discarded because of mechanical flexure and/or poor tracking in our direct drive fork mounts, which were early prototypes that we overloaded. These issues were ultimately resolved by upgrading to a next generation of mounts with increased carrying capacity.

Acknowledgments

We are thankful for contributions from the Dunlap Institute (funded through an endowment established by the David Dunlap family and the University of Toronto) which made this research possible. This research made use of Astropy, a community-developed core Python package for Astronomy (Astropy Collaboration et al. 2013, 2018). We acknowledge the support of the Natural Sciences and Engineering Research Council of Canada (NSERC). Nous remercions le Conseil de recherches en sciences naturelles et en génie du Canada (CRSNG) de son soutien. We thank the Canada Foundation for Innovation (CFI) for their support.

Software: astropy (Astropy Collaboration et al. 2013, 2018), Source Extractor (Bertin & Arnouts 1996).

Appendix A
The "Spectral Acceptance Field of View"

The bandpass of a narrowband interference filter depends on the incident angle. Incident light is collimated when placing an interference filter at the front of the aperture, which allows for much narrower filters than those on traditional telescopes which place them in a converging beam. The DSLM design places the filter at the front of the aperture, and tilts the filter to change the incident angle with respect to to the filter, thus changing the central wavelength of the filter bandpass. However with a sufficiently large FOV, the effect of the varying incident angles purely due to the FOV at the aperture becomes significant. This effect becomes more pronounced when the filter itself is tilted with respect to the optical axis.

The effective central wavelength λ of a tilted interference filter is given by:

$$\lambda = \lambda_0 \sqrt{1 - \left(\frac{1}{n_c} \sin\theta\right)^2}, \tag{A1}$$

where λ_0 is the central bandpass at 0°, θ is the tilt angle relative to the incoming wavefront (measured from a vector perpendicular to the surface of the filter), and n_c is the index of refraction of the filter (Lokhorst et al. 2020). The angle of the incoming wavefront varies across the FOV, resulting in a change in the central wavelength as a function of field angle. As per Equation (A1), the filter's central bandpass changes slowly at small tilt angles, and quickly at large tilt angles.

Because the FOV of the instrument is large (∼2° for 120 lens design described in the present paper, and ∼3° for the upcoming 1140 lens version), at large tilts, the effective central

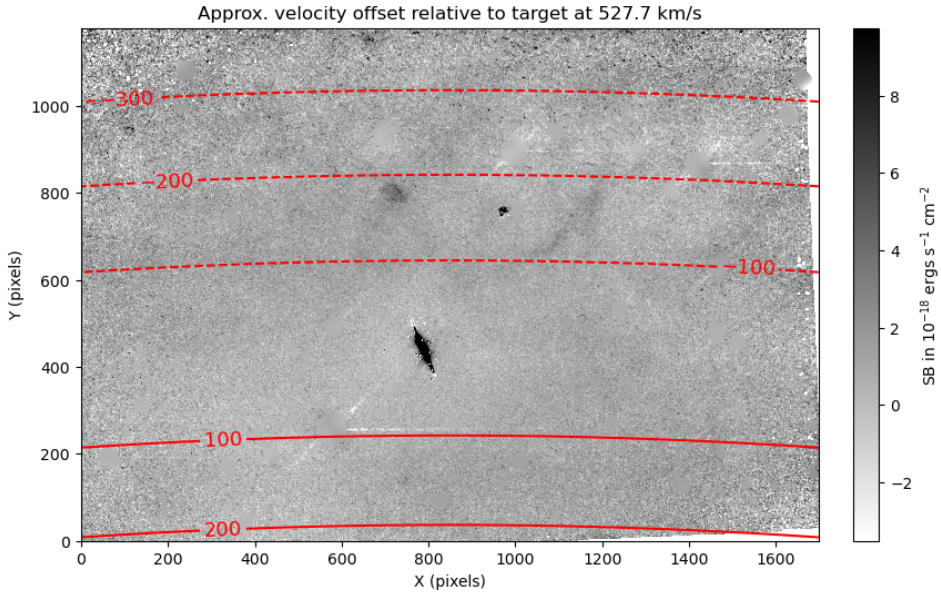

Figure 19. The NGC 891 Hα continuum subtracted and masked Hα map from Figure 10, but plotted in pixel space to keep consistent with other figures in this section. The approximate average velocity offset relative to the target velocity is show in the red contours (-300, -200, -100, 100, 200) in units of km s^{-1}. Note the spectral resolution of the 0.8 nm bandpass Hα filter is equivalent to approximately 400 km s^{-1}.

wavelength of the filter can be displaced from the on-axis central wavelength of the filter by more than the bandpass of the filter. As long as the tilts are small ($<10^{\circ}$) the effect is small, and the DSLM can best be thought of as a tunable narrow band imager. However, at larger tilts, the bandpass shift across the FOV can be become quite pronounced and the instrument is best thought of as an integral field spectrometer with a very wide FOV.

One case that clearly demonstrates the importance of considering the non monochromatic FOV is the discovery of the galactic Hα "blob" around NGC 891. As previously discussed in the text, the blob is at a velocity of 58 km s^{-1}, and NGC 891 has a recessional velocity of 528 km s^{-1}. As shown in Figure 19, the average velocity offset, with respect to the target's velocity, ranges between $+200$ and -400 km s^{-1} in the final data stack.[12] The filters have an effective velocity resolution of about 400 km s^{-1}, and with a velocity offset of approximately -200 km s^{-1} at the location of the blob, this gets the zero velocity galactic Hα on the edge of the filter.

Another way to illustrate this is to look at the filter transmission for a spectral line at a given velocity, when the filter is at a specific tilt, as shown in Figure 20. We define the "spectral acceptance FOV," or SAF for short, as the wide stripe of pixels on the FOV where the transmission for a line of interest is above a threshold transmission value. For example, a 10% SAF is useful when thinking of where it is possible to detect any emission at a given velocity/wavelength, but a 80% SAF would be used for where we would "trust" the line is "in band." When tilting to 17° to target the 528 km s^{-1} Hα line, we can see that the 58 km s^{-1} SAF creep in at the top of the FOV. Also, the additional uncertainty in the filter tilter calibration and tilt accuracy, this functionally "spreads out" or "broadens the wings" of the SAF in a stacked image coming from numerous lenses. Taking into account the non-monochromatic FOV, it is easy to explain why galactic Hα can appear in parts of an image when targeting Hα at $\sim$500 km s^{-1}, with a filter width of $\sim$400 km s^{-1}. In future work, this non-monochromatic FOV will need to be handled much more carefully. Ideally at tilts above 10°, DSLM data is cropped according to the SAF at the velocities of interest, before stacking with cropped frames with the same velocity. If sky lines are present in the field, they can be use to inform the true tilt of the filter to make more accurate crops of the SAF.

[12] Note, due to the filter tilter calibration method (see Lokhorst et al. 2024), the filter is calibrated to where the target is located in the field rather than the center of the FOV. When the images are then stacked, provided that the calibration is accurate, the velocity offsets are approximately the same relative to the target. This is because at small difference in the filter incident angle, the change in central wavelength is effectively linear.

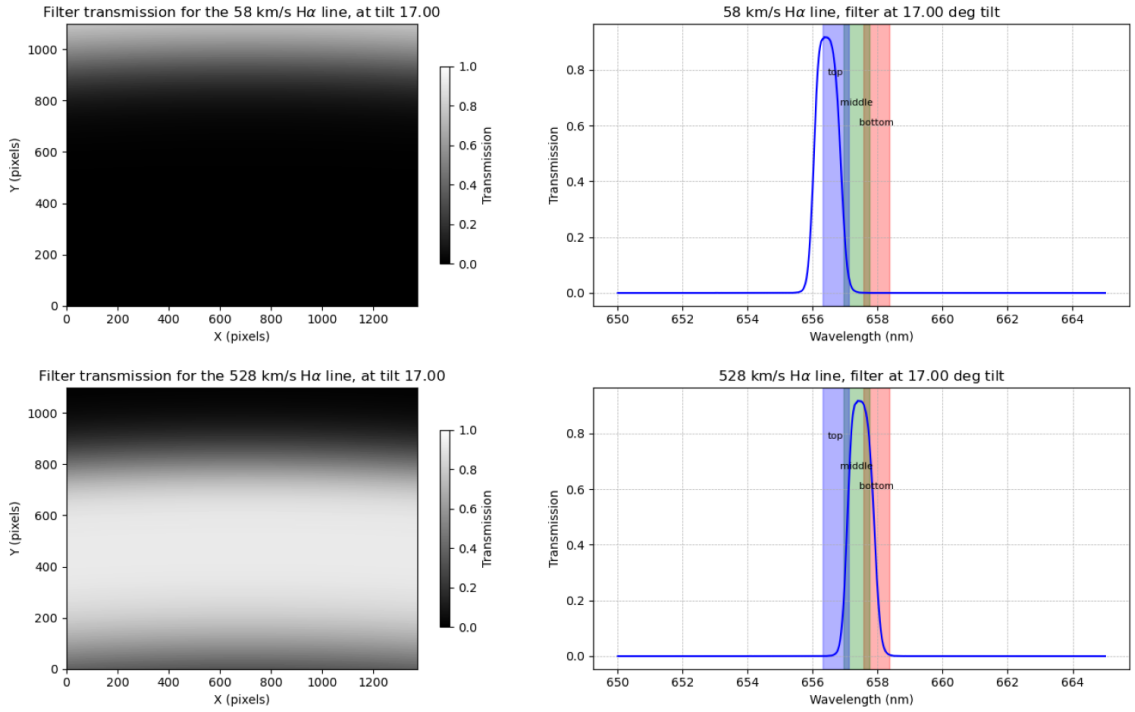

Figure 20. The filter transmission at each pixel for the Hα line at 58 km s^{-1} (top left) and at 528 km s^{-1} (bottom left), when the filter is tilted to 17°. At this tilt, the filter targets the Hα line at 528 km s^{-1} (matched to the target location in the NGC 891 field, see Figure 19). Near the top edge of the FOV, Hα emission at 58 km s^{-1} can pass through. These velocities were chosen as these are the recessional velocities of NGC 891 and the newly discovered Hα blob near NGC 891. The top right and bottom right plots show the Hα lines at the respective velocities convoluted with our Hα filter bandpass. The blue, green and red bars shows the simplified filter bandpass in the top, middle, and bottom of the frame respectively.

Appendix B
Sky Subtraction: Sky Lines and Light Leak

A result of the non-monochromatic FOV is that sky lines mostly appear as horizontal stripes across our FOV as the changing bandpass shifts them into and out of the bandpass. The higher the filter tilt, the narrower the sky line stripes are, as the central bandpass shift as a function of angle increase with the tilt angle nonlinearly. Figure 21 shows the expected sky and bandpass across the FOV, where the filter is at 10° tilt. Compared to Figure 22, where the filter is at 18.°29 tilt (corresponding to Hα at zero recessional velocity), we can see there are more skylines at high tilt, and the bandpass changes more across the FOV.

The main difference between the reduction of the DLSM data set in this paper and any previous Dragonfly data was the method of sky modeling. In the original pipeline, we use a 2D 3rd-order polynomial to model the sky, but this was insufficient in modeling both the horizontal stripes of skylines and a light leak affecting the right half of our frame (see Figure 23). After masking sources, we modeled the sky line gradient by averaging pixels less affected by the light leak over the *X*-axis to get sky counts as a function of position along the *Y*-axis. This is then fit by a 9th order polynomial. After subtracting out this one-dimensional gradient from the frame, we modeled the light leak by fitting individual rows with a 7th order polynomial, then fitting the columns with a third order polynomial to smooth out the light leak model. This method successfully removes both the sky line and the light leak from individual frames. However in stacks of many frames, "stripey" residuals may remain if targets are near strong skylines. We also lose features on scales larger than approximately 20′ with this procedure, as it is difficult to model out the light leak without over fitting the sky background on large scales.

The light leak we discovered contributes significantly to our background. It affects the entire frame but visually appears as a sharp gradient on the right side of the frame, see Figure 23. We tested the addition of a UVIR blocking filter to the back of the lens (there is filter holder built into the back of the Canon telephoto lens before the camera) and found it gets rid of the light leak while keeping source counts the same. Comparing frames with and without the UVIR blocking filter, source counts stay approximately the same while sky counts are on average doubled in the frames without the UVIR filter. While the exact cause of the light leak is not yet determined, it was likely caused by a

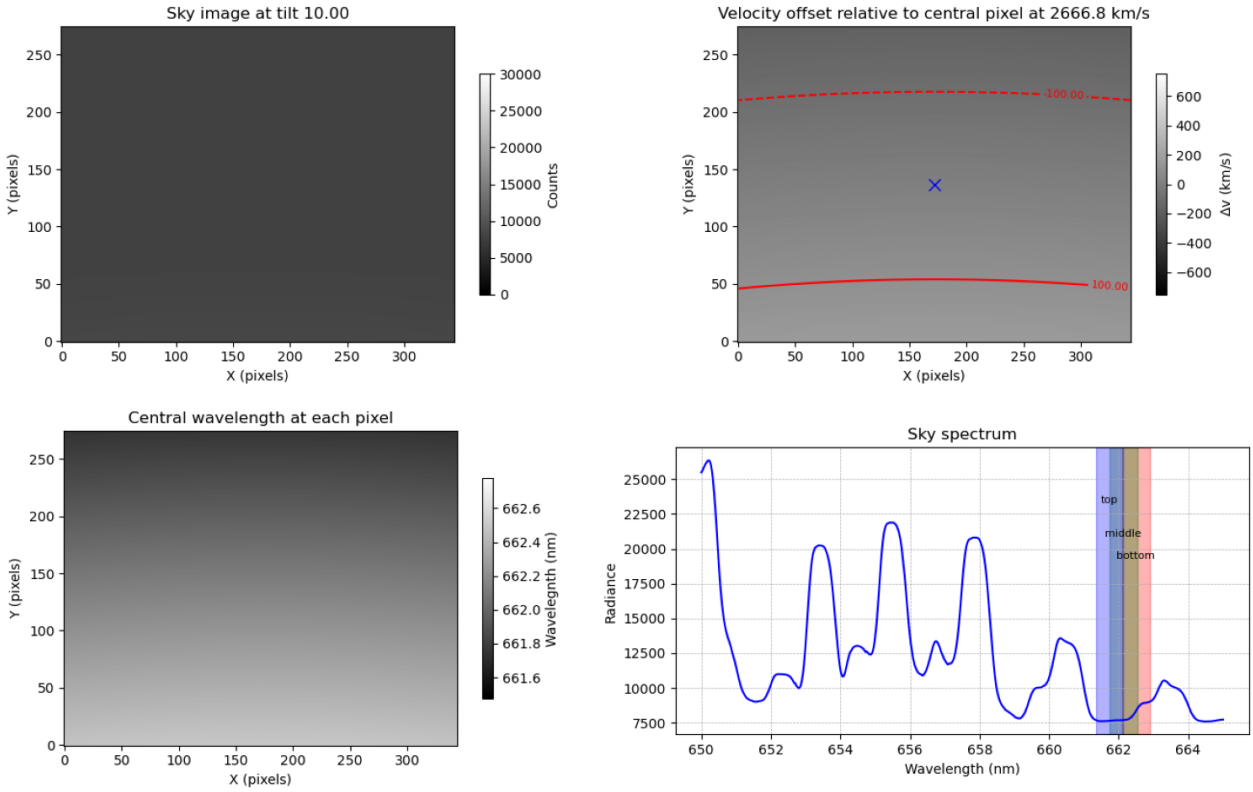

Figure 21. Upper left: simulated sky background observed by one lens of DSLM at a 10° tilt, where the counts are an arbitrary value, and tilt refers to the angle the surface normal of the filter makes with respect to the optical axis, binned 4 × 4. Upper right: the velocity offset of each pixel to the central pixel, calculated from the bottom left plot. Bottom left: the central wavelength of the effective filter bandpass for each pixel. Bottom right: the blue line shows the UVES sky spectrum convolved with our Hα filter bandpass. The blue, green, and red bars shows the simplified filter bandpass at the top, middle, and bottom of the frame respectively. Note the green bar is difficult to see due to the larger overlap at lower tilts, see Figure 22 for an example at higher tilts where there is less overlap.

component (perhaps a motor) between the front interference filter and the back of the lens producing thermal emission. As the UVIR blocking filter does an excellent job of getting rid of the light leak while maintaining excellent throughput in the optical, the exact cause of the light leak is not a priority. While too late for the data set in this paper, the addition of UVIR blocking filters to the back of the lenses will greatly improve future data quality.

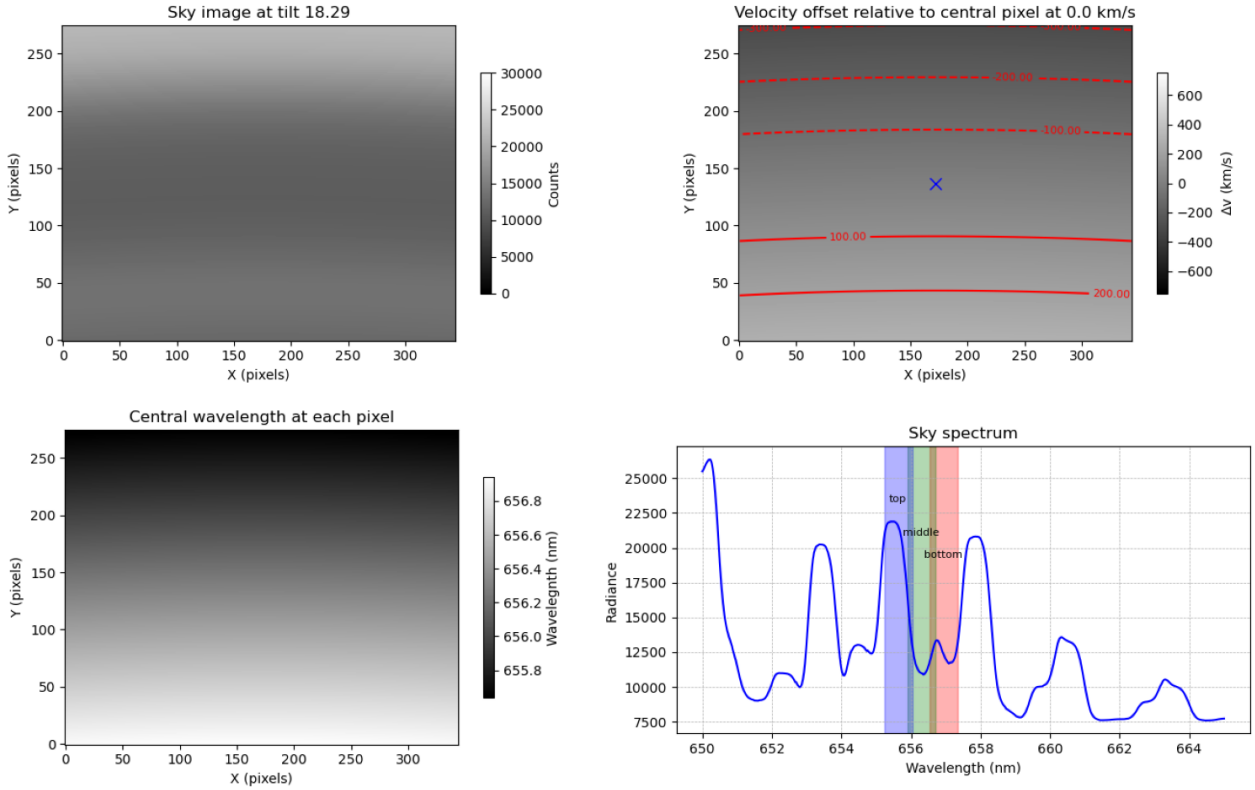

Figure 22. Same as Figure 21 but where the filter tilt (angle of the surface normal of the filter with respect to the optical axis) is 18.°29.

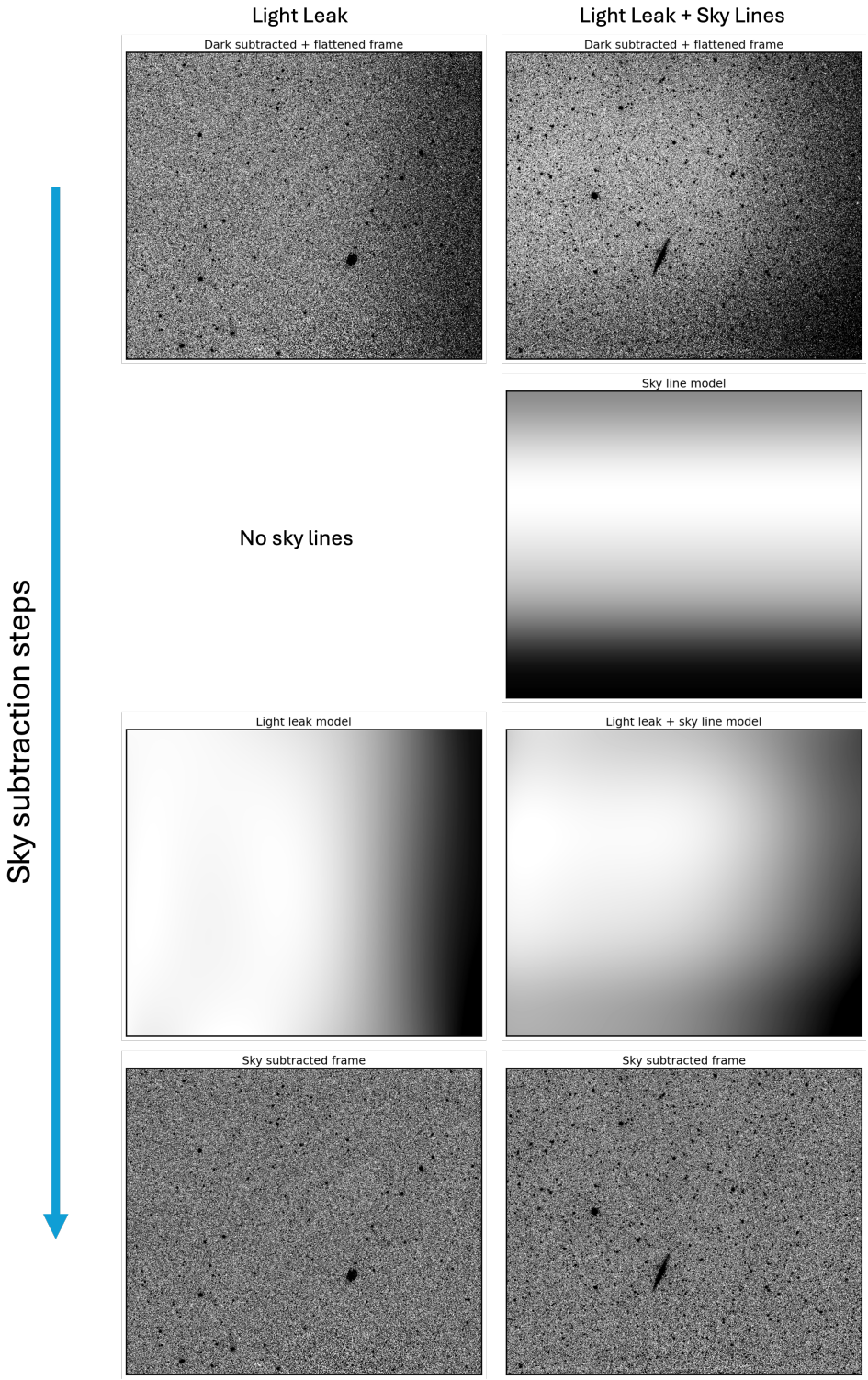

Figure 23. Sky subtraction steps to take dark subtracted and flat fielded individual frames to sky subtracted frames. On the left is a frame where there are no sky lines in the bandpass at the target tilt. On the right is a frame with a sky line on the edge of the bandpass, as seen by the darker stripe along the top. Both frames have the light leak feature on the right side of the frame. The brightness of the light leak varies with time, and lens unit, but stays on the right side of the frame in the same approximate position. Sky lines are modeled as a gradient that only varies in y pixel. The light leak is modeled through a two step higher order row, lower order column polynomial. These two steps together form the "sky" that is subtracted in the sky subtraction.

Appendix C
Photo-ionizing Flux Calculation for the NGC 6946 Panhandle

To determine the photo-ionizing flux required to produce the amount of Hα emission observed in the feature we call the panhandle in this paper, we follow the derivations of Donahue et al. (1995), Adams et al. (2011), as well as referencing (Osterbrock & Ferland 2006), Faucher-Giguère et al. (2009) and Fumagalli et al. (2017). The surface brightness of an optically thick H I cloud is directly proportional to the incident ionizing photon flux. Following Donahue et al. (1995), we make the following assumptions about the H I cloud:

1. Optically thin to Hα photons,
2. Illuminated on all side so photons can be counted on both sides of the cloud,
3. Undergoing case B recombination at $\sim 10^4$ K, where the fraction of incident ionizing photons converted to Hα photons is $f_{\mathrm{H}\alpha} \sim 45\%$.

The $\sim$45% value is from the Hα effective recombination coefficient $\alpha^{\mathrm{eff}}_{\mathrm{H}_\alpha}$ divided by the case B recombination coefficient α_B. At $T = 10^4$ K and and electron density of $n_e \approx 1\,\mathrm{cm}^{-3}$, $\alpha^{\mathrm{eff}}_{\mathrm{H}_\alpha} = 11.7 \times 10^{-14}\mathrm{cm}^3\,\mathrm{s}^{-1}$ and $\alpha_B = 2.59 \times 10^{-14}\,\mathrm{cm}^3\,\mathrm{s}^{-1}$. In equation form, this is written as

$$Q_{\mathrm{H}\alpha} = \frac{\alpha^{\mathrm{eff}}_{\mathrm{H}_\alpha}}{\alpha_B} Q_{\mathrm{H}_0} \tag{C1}$$

where $Q_{\mathrm{H}\alpha}$ and Q_{H_0} are the number of Hα and ionizing photons respectively.

We also account for two correction factors:

1. The geometrical correction factor f_g, where f_g is 1 for a sphere, $4/\pi$ for a long narrow cylinder, 2 for a face on slab, or $2\cos\theta$ for a slab inclined at angle θ with respect to the observer.
2. The spectral shape factor f_s. If the UVB specific intensity is given by $J_\nu = J_0\left(\frac{\nu}{\nu_0}\right)^{-\beta}$, then $f_s = \frac{1}{\ln(4)}$ for $\beta = 0$ and $f_s = \frac{\beta}{1-4^{-\beta}}$ for $\beta > 0$. The spectral index β used by Donahue et al. (1995) and Fumagalli et al. (2017) is 0.5 and 1.8 respectively. More recent simulations of the UVB (Haardt & Madau 2012; Khaire & Srianand 2019; Faucher-Giguère 2020) all place the value of β to be $\sim$2 for ionizing photons 1–10 Ryd, and $\sim$0.5 for photons 10–1000 Ryd.

Then the specific radiative intensity of the ionizing background at the Lyman limit (1 Ryd, 13.6 eV) can be approximated by the following equation

$$J_0 = \frac{h\Phi_{\mathrm{H}\alpha}}{f_{\mathrm{H}\alpha}} f_g f_s \tag{C2}$$

The photoionization rate is given by

$$\Gamma = 4\pi \int_{\nu_0}^{\infty} \frac{J_\nu \sigma_\nu}{h\nu} d\nu. \tag{C3}$$

and with σ_ν approximated by a power law $\sigma_\nu = \sigma_0\left(\frac{\nu_0}{\nu}\right)^3$ for $h\nu \geqslant 13.6$ eV, integrating over range of ionizing photons frequencies we get:

$$\Gamma = \frac{4\pi\sigma_0 J_0}{h(3+\beta)}. \tag{C4}$$

Combining Equations (C2) and (C4), we get:

$$\Gamma = \frac{4\pi\sigma_0}{3+\beta} \frac{f_g f_s}{f_{\mathrm{H}\alpha}} \Phi_{\mathrm{H}\alpha} \tag{C5}$$

For our panhandle flux of $5.4 \times 10^{-18}\,\mathrm{erg\,s^{-1}\,cm^{-2}\,arcsec^{-2}}$, assuming a spherical geometry with $f_g = 1$ and $\beta = 1.8$, this corresponds to a photoionization rate of $\Gamma = 5.9 \times 10^{-12}\,\mathrm{s}^{-1}$. For a face on slab with $f_g = 2$ and $\beta = 1.8$, this corresponds to $\Gamma = 1.2 \times 10^{-12}\,\mathrm{s}^{-1}$. Regardless of the geometry, these photoionization rates are two orders of magnitude greater than the UVB photoionization rate predicted by simulations (Faucher-Giguère et al. 2009; Haardt & Madau 2012; Khaire & Srianand 2019; Faucher-Giguère 2020) with $\Gamma = 2$–$5 \times 10^{-14}\,\mathrm{s}^{-1}$, and the lower limit from observation (Fumagalli et al. 2017) where $\Gamma = 6$–$10 \times 10^{-14}\,\mathrm{s}^{-1}$. Therefore, another source of ionization is required.

ORCID iDs

Seery Chen https://orcid.org/0000-0002-4175-3047
Deborah M. Lokhorst https://orcid.org/0000-0002-2406-7344
Imad Pasha https://orcid.org/0000-0002-7075-9931
William P. Bowman https://orcid.org/0000-0003-4381-5245
Steven R. Janssens https://orcid.org/0000-0003-0327-3322
Carter Rhea https://orcid.org/0000-0003-2001-1076
Qing Liu https://orcid.org/0000-0002-7490-5991
Zili Shen https://orcid.org/0000-0002-5120-1684
Roberto G. Abraham https://orcid.org/0000-0002-4542-921X
Pieter van Dokkum https://orcid.org/0000-0002-8282-9888

References

Abraham, R. G., & van Dokkum, P. G. 2014, PASP, 126, 55
Adams, J. J., Uson, J. M., Hill, G. J., & MacQueen, P. J. 2011, ApJ, 728, 107
Astropy Collaboration, Price-Whelan, A. M., Sipőcz, B. M., et al. 2018, AJ, 156, 123
Astropy Collaboration, Robitaille, T. P., Tollerud, E. J., et al. 2013, A&A, 558, A33
Bekiaris, G., Glazebrook, K., Fluke, C. J., & Abraham, R. 2016, MNRAS, 455, 754
Bertin, E., & Arnouts, S. 1996, A&AS, 117, 393

Bigiel, F., de Looze, I., Krabbe, A., et al. 2020, ApJ, 903, 30
Boomsma, R., Oosterloo, T. A., Fraternali, F., van der Hulst, J. M., & Sancisi, R. 2008, A&A, 490, 555
Cedres, B., Cepa, J., Bongiovanni, A., et al. 2012, yCat, J/A+A/545/A43. Originally published in: 2012A&A...545A..43C, J/A+A/545/A43
Chen, S., Lokhorst, D. M., Pasha, I., et al. 2024, Proc. SPIE, 13094, 130942J
Chen, S., Lokhorst, D. M., Shen, J., et al. 2022, Proc. SPIE, 12182, 121824E
Danieli, S., Lokhorst, D., Zhang, J., et al. 2020, ApJ, 894, 119
Das, S., Rickel, M., Leroy, A., et al. 2024, MNRAS, 527, 10358
Dettmar, R. J. 1990, A&A, 232, L15
Donahue, M., Aldering, G., & Stocke, J. T. 1995, ApJL, 450, L45
Falco, E. E., Kurtz, M. J., Geller, M. J., et al. 1999, PASP, 111, 438
Faucher-Giguère, C.-A. 2020, MNRAS, 493, 1614
Faucher-Giguère, C.-A., Lidz, A., Zaldarriaga, M., & Hernquist, L. 2009, ApJ, 703, 1416
Ferguson, A. M. N., Gallagher, J. S., & Wyse, R. F. G. 1998, AJ, 116, 673
Fraternali, F., & Binney, J. J. 2008, MNRAS, 386, 935
Fumagalli, M., Haardt, F., Theuns, T., et al. 2017, MNRAS, 467, 4802
Haardt, F., & Madau, P. 2012, ApJ, 746, 125
Haffner, L. M., Reynolds, R. J., Tufte, S. L., et al. 2003, ApJS, 149, 405
Hanuschik, R. W. 2003, A&A, 407, 1157
Heesen, V., O'Sullivan, S. P., Brüggen, M., et al. 2023, A&A, 670, L23
Henden, A. A., Templeton, M., Terrell, D., et al. 2016, yCat, II/336. Originally published in: 2015AAS...22533616H, II/336
Holt, S. S., Schlegel, E. M., Hwang, U., & Petre, R. 2003, ApJ, 588, 792
Huchra, J. P., Vogeley, M. S., & Geller, M. J. 1999, ApJS, 121, 287
Keim, M. A., van Dokkum, P., Danieli, S., et al. 2022, ApJ, 935, 160
Khaire, V., & Srianand, R. 2019, MNRAS, 484, 4174
Lan, T.-W., & Prochaska, J. X. 2020, MNRAS, 496, 3142
Lokhorst, D., Abraham, R., Pasha, I., et al. 2022, ApJ, 927, 136
Lokhorst, D., Abraham, R., van Dokkum, P., Wijers, N., & Schaye, J. 2019, ApJ, 877, 4
Lokhorst, D. M., Abraham, R. G., van Dokkum, P., & Chen, S. 2020, Proc. SPIE, 11445, 1144527
Lokhorst, D. M., Chen, S., Pasha, I., et al. 2022, Proc. SPIE, 12182, 121821T
Lokhorst, D. M., Chen, S., Pasha, I., et al. 2024, Proc. SPIE, 13094, 130942N
Morisset, C., Delgado-Inglada, G., & Flores-Fajardo, N. 2015, RMxAA, 51, 103
Oke, J. B., Cohen, J. G., Carr, M., et al. 1995, PASP, 107, 375
Oosterloo, T., Fraternali, F., & Sancisi, R. 2007, AJ, 134, 1019
Osterbrock, D. E., & Ferland, G. J. 2006, Astrophysics of Gaseous Nebulae and Active Galactic Nuclei (Univ. Science Books)
Pakmor, R., van de Voort, F., Bieri, R., et al. 2020, MNRAS, 498, 3125
Rand, R. J. 1997, ApJ, 474, 129
Rand, R. J., Kulkarni, S. R., & Hester, J. J. 1990, ApJL, 352, L1
Sancisi, R., & Allen, R. J. 1979, A&A, 74, 73
Strickland, D. K., Heckman, T. M., Colbert, E. J. M., Hoopes, C. G., & Weaver, K. A. 2004, ApJS, 151, 193
Westmeier, T. 2018, MNRAS, 474, 289
Yadav, J., Das, M., Patra, N. N., et al. 2021, ApJ, 914, 54